DELFT UNIVERSITY OF TECHNOLOGY

MASTER THESIS

Optimization of Cantilever-Shaped Piezoelectric Energy Harvester

— with the Application of Mechanical Stoppers

Author:
Yuchen CHEN

Supervisor:
Prof.dr.ir. Sybrand van der ZWAAG
Ir. Dimosthenis GIANNOPOULOS
Prof.dr. DirkJan VEEGER

A thesis submitted in fulfillment of the requirements for the degree of Master of Science

in the

Bio-Mechanical Design
Mechanical, Maritime and Materials Engineering

Student ID 4798333

Thesis Committee

Prof.Dr. H.E.J. Veeger	*3mE*, TU Delft
Prof.Dr.Ir. S. van der Zwaag	*AE*, TU Delft
Prof.Dr. P.J. French	*EEMCS*, TU Delft
Ir. D. Giannopoulos	*AE*, TU Delft

September 25, 2020

Abstract

Energy harvesting has become a popular topic for battery substitution in recent years. In particular, mechanical vibrational energy, one of the most common energy sources, has been intensely studied. Piezoelectric materials play a crucial role in vibrational energy harvesting as they can directly convert the mechanical energy to the desired electric energy. In particular these are attractive when they are made into a cantilever form allowing the harvester to harness larger energy. This project aimed at optimizing the performance of single-layered piezoelectric cantilevers, also known as the unimorphs, from the point of view of output power and operation lifetime with the use of a stroke limit stopper.
In this study, a cantilever beam consisting of PZT (PZT5A4) bonded to an elastic substrate (Pernifer 45) with a tip mass attached to the free end is used as the harvester. To reduce the cracks generated in the piezoelectric material and subsequently increase the lifetime, a limit stopper is introduced to constrain the deflection of the unimorph.The influence of the stroke on the lifetime and power output is shown by a series of vibration tests under different operation conditions with varied unimorph lengths, configurations, attached tip masses and stroke distances. The result confirms the possibility of the limit stopper to improve output energy of longer unimorphs in certain distance ranges. It also points out that current designs do not allow performance optimization in both output and lifetime simultaneously. One ought to choose one of the two, as the methods which increased the instant power output also resulted in a sharp reduction in lifetime as well as total power capacity.

Acknowledgements

This thesis was done in the fulfillment of the requirement for the Master track Biomechanical Design in Mechanical, Maritime and Materials Engineering Department at Delft University of Technology, the Netherlands, and was carried out at the Novel Aerospace Material group of the Aerospace Engineering Department at TU Delft. The completion of this thesis would not have been possible without the guidance and assistance from those who provide backing along my research. For this reason, I would like to express my gratitude towards them.

First and foremost, I would like to thank Prof. Sybrand van der Zwaag for taking over the supervision and his guidance and advice throughout the project for exploring new concepts and strategies for tackling the problems. His expertise and encouragements were pivotal to my research and taught me to become a better researcher.

Besides, I would like to show my gratitude towards Prof. DirkJan Veeger for his support from the very beginning of the project and the mentorship all along. I am particularly grateful for the acceptance from Prof. Pim Groen, who kindly offered me this opportunity to work on the project. I would also like to thank my Ph.D supervisor, Dimosthenis Giannopoulos, for his patience and enthusiasm in helping me with all the problems I've encountered. Special thanks to Dr. Tadhg Mahon for providing insightful advices and technical helps during the research.

Finally, I would like to express my gratitude to my family and friends for supporting and continuous encouraging me throughout my study and the process of researching. This accomplishment would not have been possible without them.

Yuchen Chen
Delft,September 2020

Contents

List of Figures

List of Tables

List of Symbols

A	cross-section area	m^2
C	capacitance	$F\ (A^2\,s^4\,kg^{-1}\,m^{-2})$
D	electric displacement	$C\,m^{-2}$
E	Young's modulus	$N/m^2\ (kg\,m^{-1}\,s^{-2})$
E_c	electric field	$V\,m^{-1}$
E_{life}	power capacity	J
F	force	N
I	current	A
L	unimorph length	m
M_t	tip mass	kg
P	power	$W\ (J\,s^{-1})$
R	resistance	Ω
S	strain	–
T	stress	$N/m^2\ (kg\,m^{-1}\,s^{-2})$
V	voltage	V
c	damping	$N\,s\,m^{-1}$
d	cantilever deflection	m
d_{ij}	piezoelectric charge constant	$C\,N^{-1}\ (m\,V^{-1})$
f	frequency	Hz
f_n	natural frequency	Hz
g	piezoelectric voltage constant	$V\,m\,N^{-1}\ (m^2\,C^{-1})$
h	stopper distance	m
k	stiffness	$kg\,s^{-2}$
m	total mass	kg
r	ordinal number of vibration	–
s	compliance	$m^2\,N^{-1}$
t	material thickness	m
w	unimorph width	m
ϵ	absolute permittivity	$F\,m^{-1}$
ω	angular frequency	rad
ω_n	natural angular frequency	rad
ν	Poisson's ratio	–
ζ	damping ratio	–

Chapter 1

Introduction

With the rapid development of the Internet of Things (IoTs) and Microelectromechanical systems (MEMS), wireless sensor technology has become more popular in many applications. As needs for portable devices arise, problems of energy supply occur due to the stagnant improvement of the traditional energy source, batteries[1][2], as shown in Fig.1.1. As a result, scaling down the electronic devices is often restricted by the batteries, whose performance in terms of power efficiency and storage capacity decline greatly alongside with the size reduction[3]. To solve the issue, intensive research has been carried out in the past few years, and piezoelectric materials have attracted much attention due to their considerable potential in extracting energy from diverse sources such as fluid flow, infrastructure, vehicles, living bodies, to name but a few.

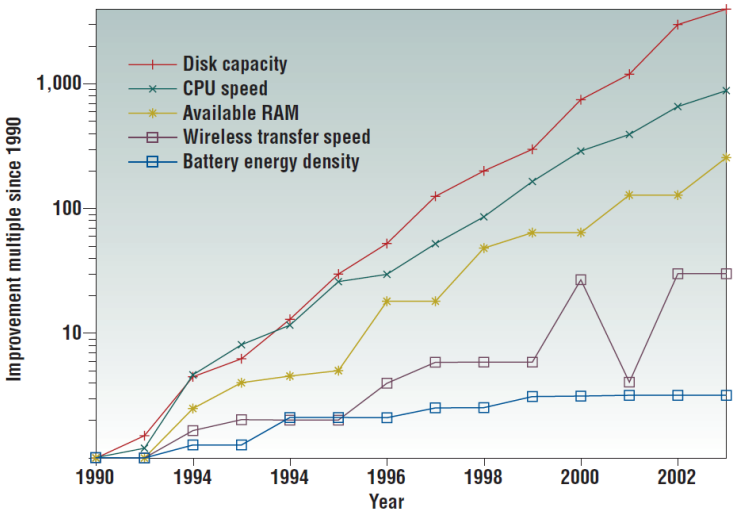

FIGURE 1.1: Relative improvement of electronics[4]

Energy harvesting is defined as the conversion of ambient wasted energy into electrical energy through a transduction mechanism[5][6]. Research has been conducted to study various types of energy sources, and their power densities are illustrated in Fig.1.2. Vibration mechanical energy, despite not being the most power intensive energy source, has been extensively studied on account of its abundance and effectiveness in energy conversion. The cantilever shape of energy harvesters is developed for the piezoelectric materials to effectively extract energy from vibration due to its

high flexibility and sensitivity. Comprehensive models were built by researchers and various approaches to improve output power were introduced throughout the literatures over past 20 years.

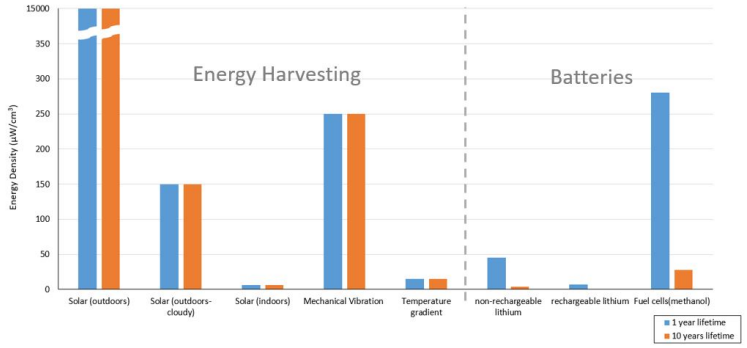

FIGURE 1.2: Power density of current available energy sources[7]

Problem statement

Another significant aspect of the harvester performance, apart from the diverse innovation in output improvement, is the durability of the design and the system. There are few currently available approaches to improve the harvester durability, mostly being limited to the mechanical stoppers and external compressive strain to the harvesters. Of these, the stoppers are, generally, more widely adopted in systems to improve harvester output performance instead. This piqued our curiosity as to whether the stopper is able to play the role of protection and output improvement at the same time. This leads to the objective of the research:

Optimize the performance of the piezoelectric cantilever design in the view of both power output and lifetime by adopting a mechanical stopper.

To achieve this objective, the research questions are formed:

How would the stoppers help improve the piezoelectric cantilever output and lifetime?

As it is known that tip mass plays a key role in unimorph performance, would the influence from the stopper be more effective than tip mass?

In order to understand the effects caused by the stopper, one needs to know the original vibration behavior of the unimorphs in advance, and different sample conditions are adopted to test the performance and tendencies of the unimorphs. Variables in sample condition of this study include unimorph length, mass of the attached tip mass, and the cantilever configuration. In this study, we propose a curved cantilever for testing, for that it is expected to be prone to one-side deflection due to its inward-bending shape, which, hopefully, could increase the output. Based on the research question, this research was separated into two parts - vibration with strokes and vibration without strokes, and both conditions would be tested under two schemes, life length and the power generation.

Thesis structure

This thesis report starts with chapter 2 of background knowledge, from the fundamental principle of piezoelectric effect and piezoelectric materials, to literature review on piezoelectric vibrational energy harvesting. Chater 3 discusses about the material and machine used, and introduces the concepts and methods adopted in the two parts of experiments. Following is the result and discussion chapter 4, which presents and analyzes the measurement results from the experiments, and provides comparison to the performance in the view of two – lifetime and output - domains. This entire project was concluded in the chapter 5, which summarizes the project and offers recommendations for future studies.

Chapter 2

Background Knowledge

2.1 Piezoelectricity

The term piezoelectricity came from the combination of two ancient Greek words: “piezein”, meaning to press or squeeze, and “elecktron”, meaning amber (the material attracts others once rubbed), and literally means “the electricity by pressing”[8].

2.1.1 Piezoelectric effect and coefficients

The piezoelectric effect was first discovered by Jacques and Pierre Curie in 1880[9], and the next year they verified the inverse piezoelectric effect[8], predicted mathematically from thermodynamic principles by Gabriel Lippmann. The general effect describes a material behavior that converts mechanical energy into electrical energy and vice versa. The reversibility of conversion direction forms the two principal effects: the direct piezoelectric effect and the inverse piezoelectric effect, as illustrated in Fig.2.1.

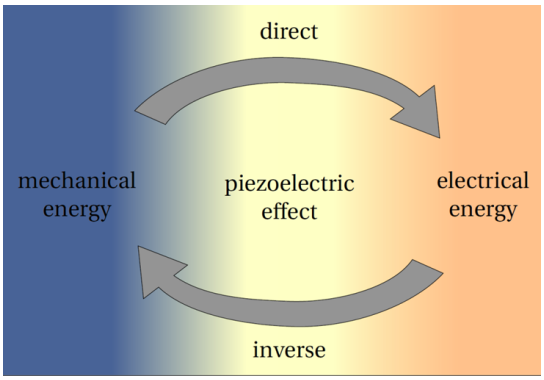

FIGURE 2.1: The direct and inverse piezoelectric effects

Fig.2.2 depicts the behavior of a piezoelectric material in a exaggerated manner. The direct piezoelectric effect refers to the phenomenon of electric charge generation of a material under mechanical stress. As shown in Fig.2.2(a), when the material is subjected to an external strain, it results in the presence of electric charge, and the direction of the charge relies on the direction of the force applied. The inverse piezoelectric effect, on the other hand, describes that the material experienced strain when

electric field was applied[8], as shown in Fig.2.2(b). Subjected to the electrical field, the material is either lengthened or shortened in the aligned direction, depending on the polarity of the field applied. Note that the dimensions in the perpendicular direction also change (via Poisson's ratio) accordingly.

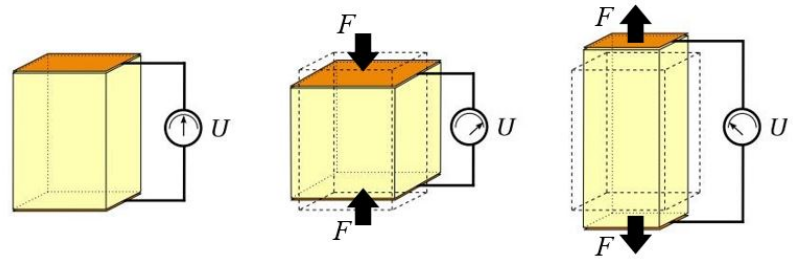

(a) Direct piezoelectric effect in a rectangular shaped component

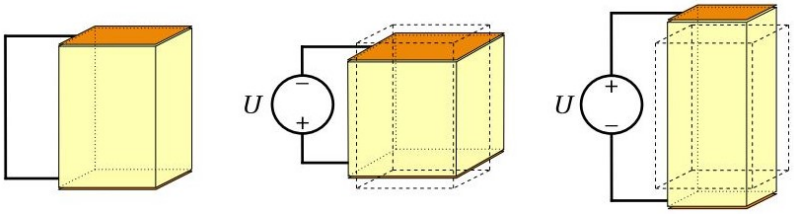

(b) inverse piezoelectric effect

FIGURE 2.2: Schematic concept of piezoelectric effect[8]

The constitutive equation of the linear piezoelectric effect could be written as:

$$\begin{cases} S = s^E T + dE \\ D = dT + \epsilon^T E \end{cases} \tag{2.1}$$

where
S: strain [-], the relative deformation
T: stress[N/m^2], force per unit area
E: electric field [V/m],
s: compliance [m^2/N] of material (strain per unit stress)
ϵ [F/m]: absolute permittivity of the material
d: piezoelectric charge constant [C/N](=[m/V])
Superscripts denotes the electric and mechanical boundary conditions. While ϵ^T [F/m] stands for permittivity under constant stress $\vec{T}$, s^E meant the compliance under constant electric field $\vec{E}$.
Due to the anisotropic nature of the piezoelectric material, the parameters listed above are regarded as tensors to accurately describe the piezoelectric behavior in space, with the assignation of axes and directions of deformation aligned with the poling direction (defined as the 3 direction), as the Fig.2.3 showed.
The strain $\vec{S}$ and stress $\vec{T}$ are vectors composed of six elements, 3 for normal deformation and 3 for shearing deformation; the electric displacement $\vec{D}$ and electric field $\vec{E}$ were vectors, each consisting of three elements, related to the three normal axes.

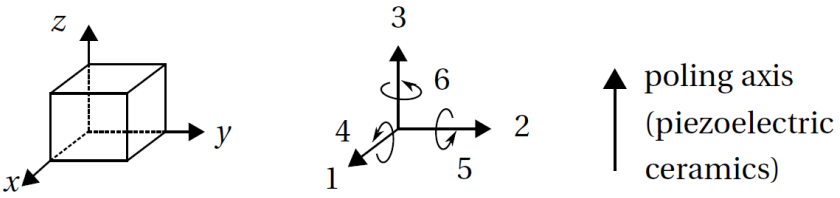

FIGURE 2.3: The designated axes and directions of the piezoelectric behavior[8]

The complete piezoelectric, elastic and electric behavior in matrix notation then becomes:

$$\begin{pmatrix} S_1 \\ S_2 \\ S_3 \\ S_4 \\ S_5 \\ S_6 \\ D_1 \\ D_2 \\ D_3 \end{pmatrix} \begin{bmatrix} s_{11}^E & s_{12}^E & s_{13}^E & s_{14}^E & s_{15}^E & s_{16}^E & d_{11} & d_{21} & d_{31} \\ s_{21}^E & s_{22}^E & s_{23}^E & s_{24}^E & s_{25}^E & s_{26}^E & d_{12} & d_{22} & d_{32} \\ s_{31}^E & s_{32}^E & s_{33}^E & s_{34}^E & s_{35}^E & s_{36}^E & d_{13} & d_{23} & d_{33} \\ s_{41}^E & s_{42}^E & s_{43}^E & s_{44}^E & s_{45}^E & s_{46}^E & d_{14} & d_{24} & d_{34} \\ s_{51}^E & s_{52}^E & s_{53}^E & s_{54}^E & s_{55}^E & s_{56}^E & d_{15} & d_{25} & d_{35} \\ s_{61}^E & s_{62}^E & s_{63}^E & s_{64}^E & s_{65}^E & s_{66}^E & d_{16} & d_{26} & d_{36} \\ d_{11} & d_{12} & d_{13} & d_{14} & d_{15} & d_{16} & \epsilon_{11}^T & \epsilon_{12}^T & \epsilon_{13}^T \\ d_{21} & d_{22} & d_{23} & d_{24} & d_{25} & d_{26} & \epsilon_{21}^T & \epsilon_{22}^T & \epsilon_{23}^T \\ d_{31} & d_{32} & d_{33} & d_{34} & d_{35} & d_{36} & \epsilon_{31}^T & \epsilon_{32}^T & \epsilon_{33}^T \end{bmatrix} \begin{pmatrix} T_1 \\ T_2 \\ T_3 \\ T_4 \\ T_5 \\ T_6 \\ E_1 \\ E_2 \\ E_3 \end{pmatrix} \tag{2.2}$$

Subscripts of the properties refer to directions in Cartesian coordinate system [10]. For the piezoelectric charge constant d_{ij}, i and j denote the directions of the electric and mechanical quantities respectively. This designation principle of the subscripts is applied for all the other piezoelectric constants in the rest of the paper.
The equations could be expressed in matrix notation, which was regarded as the standard expression:

$$\begin{pmatrix} \vec{S} \\ \vec{D} \end{pmatrix} \begin{bmatrix} s^E & d \\ d & \epsilon^T \end{bmatrix} \begin{pmatrix} \vec{T} \\ \vec{E} \end{pmatrix} \tag{2.3}$$

As the field of energy harvesting mainly focused on the electric field yielded under the applied mechanical energy, Eq.2.1 can be better written:

$$\begin{pmatrix} \vec{S} \\ \vec{E} \end{pmatrix} \begin{bmatrix} s^D & g \\ -g & (\epsilon^T)^{-1} \end{bmatrix} \begin{pmatrix} \vec{T} \\ \vec{D} \end{pmatrix} \tag{2.4}$$

where g [Vm/N](= $[m^2/C]$) denotes the piezoelectric voltage constant, which has the relation to the charge constant described in Eq.2.5:

$$g = \frac{d}{\epsilon^T} \tag{2.5}$$

and s^D $[m^2/N]$ is the compliance under conditions of constant electric displacement D,

$$s^D = s^E - \frac{d^2}{\epsilon^T} = s^E(1 - \frac{d^2}{s^E \epsilon^T}) \tag{2.6}$$

Piezoelectric ceramics allow different modes of coupling between electrical and mechanical domains, and the dominant operation modes in energy harvesting are the d_{33}–mode and the d_{31}–mode [11]. In d_{33}–mode, also known as longitudinal operation, directions of deformation and electric field are parallel to the poling direction, the 3-axis. As for d_{31}–mode, or transverse operation, the electric field is parallel to

the poling axis (3-axis), while the deformation is perpendicular to the poling axis (subscript 1) (see Fig.2.4).

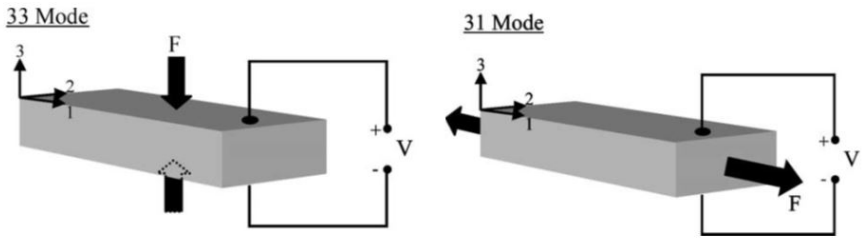

FIGURE 2.4: Operation modes d_{33} and d_{31}

Since the deformation along the poling direction causes the deformation in the perpendicular direction, the charge constant of longitudinal and transverse operation is interrelated:

$$d_{31} = -\nu d_{33} \tag{2.7}$$

where ν is the Poisson's ratio.
For the bulk piezoelectric material, the voltage induced by mechanical loads is

$$V = g_{33} \times T \times t \tag{2.8}$$

where t denotes the thickness of the material.
Therefore, the output power could be calculated as

$$P = \frac{1}{2} C V^2 \times f = \frac{1}{2} g_{33} \times d_{33} \times F^2 \frac{t}{A} f \tag{2.9}$$

where C denotes the capacitance of the transducer, F is the applied force and f refers to the frequency of the vibration. The output power could be evaluated by the product of g and d as the figure of merit of the transducer[12]:

$$P \propto g \times d \tag{2.10}$$

Note that the current constant d and voltage constant g correspond to the specific mode of operation and the structure, which should be replaced by the effective value when calculated[13].

2.1.2 Ceramics and poling

The crystal structure of the piezoelectric material contributes to the piezoelectric effect. A dielectric material, which is non-conducting and lacks a center of symmetry, has the charges inside shifted when mechanical load applied, leading to the yield of dipole. Dipole accumulation results in electric charge generation[14]. As for the inverse effect, electrical force induced by the applied electric field acts on ions, leading to displacement of the ions along with polarization, which behaves as a deformation macroscopically[8].
A considerable number of materials which exhibit piezoelectric behavior have been

discovered, and were classified as piezoelectric single crystals, piezoelectric ceramics, piezoelectric polymers, piezoelectric composites, and thin film piezoelectrics. Among them, the ceramics are one of the most commonly applied categories in energy harvesting by virtue of their large voltage output without bias voltages and capability to be made in nearly any size and shape.
Among the piezoelectric ceramics, studies mostly focus on one group of ceramics – the ferroelectric ceramics. Materials whose polarization directions could be changed by an adequately large electric field are said to be ferroelectric. One of their characteristics is they are formed in small regions with uniform polarization, known as Weiss domains. Domains are separated by domain walls and all the dipoles are aligned within each domain. The phenomenon results in a non-polarized ferroelectric crystal at a macroscopic scale, but the crystal could be given an artificial polarization in any desired direction by a process called poling. Poling is a treatment that induces the piezoelectric properties of ceramics[15]. During the treatment, domains in the ceramics are aligned by exposing the element to a strong electric field at a temperature slightly below the Curie temperature[16], the temperature above which a material loses its piezoelectric behavior.
One of the most well-known structures among the ferroelectric ceramics is the perovskite crystal structure, composed of a tetravalent metal ion, B^{4+}, which is surrounded by a lattice of divalent metal ions, A^{2+}, and oxygen ions, with the general form ABO_3.
The predominant commercial piezoelectric ceramic is the lead zirconium titanate (PZT). PZT has advantages of easy fabrication, low cost in manufacturing, and high energy conversion rate, all contributing to its domination of the piezoelectric application[17]. Piezoelectric properties of PZTs are also tailorable by diverse chemical modifications to fit different applications. For instance, PZTs attain larger electromechanical coupling factors and permittivity when doped with Nb^{5+} or Ta^{5+}, leading to larger displacement and larger signal bandwidth, and are commonly applied to sensing and energy harvesting systems; while doped with Fe^{3+} or Sc^{3+} leaded to more stable mechanical properties and high compatibility with high mechanical loads and voltage, which is preferred for use in high frequency resonance device[18][19].

2.2 Vibrational Piezoelectric Energy Harvesting

The energy harvesting process for piezoelectrics includes three basic phases, as displayed in Fig.2.5, and the piezoelectric transduction is the second phase of conversion, denoted by the yellow box in Fig.2.5. Each of the conversion steps has to be optimized to obtain the maximum performance. The initial phase involves the mechanical energy being captured by the piezoelectric transducer, including mechanically stabilizing the transducer under large stresses and mechanical impedance matching. To avoid energy transformation losses, the stiffness of the material has to be tuned to the stiffness of the overall structure. The second phase is the electromechanical conversion within the piezoelectric transducer. The optimization relies on the material selection and matching the geometry to both the mechanical and electrical conditions. In the last phase, the electrical energy is transferred from the piezoelectric transducer to the electric load, which is more complicated in diverse conditions, but also requires impedance matching[8][12].

Vibration energy harvesting, also known as inertial energy harvesting, extracts energy from the resistance to the acceleration, in which the transducer attaches to the moving structure by a single point performed in a 1 Degree of Freedom (DoF) vibration. It operates at close-to-resonant frequency to yield the maximum output, and the vibration amplitude is restricted by the energy loss due to the friction, electric coupling coefficient or damping. Since the stress is not directly applied on the transducer, inertial energy harvesting setups are more flexible in terms of their mounting and allow for higher levels of miniaturization[20][21][22].

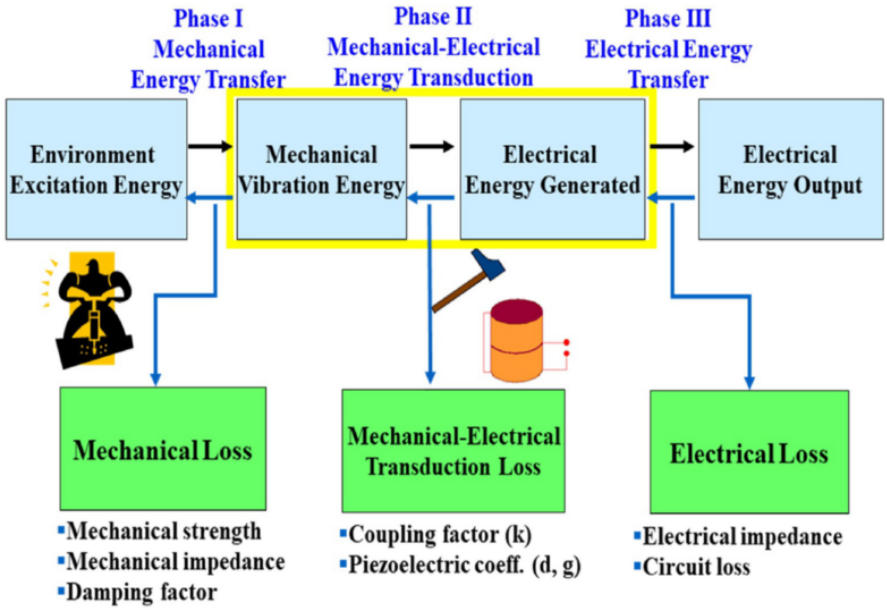

FIGURE 2.5: Three major phases associated with piezoelectric energy harvesting[12]

2.2.1 Cantilever

In order to enhance the piezoelectric transducer performance and maximize the efficiency of the energy harvesting, piezoelectric materials are designed into diverse configurations in response to various mechanical energy sources, for instance, multilayered stack, rainbow curve, or macro fibers, to name but a few. Among them, the cantilever beam configuration was the most commonly-adopted configuration in vibration energy harvesting due to its simplicity in manufacturing and modeling.

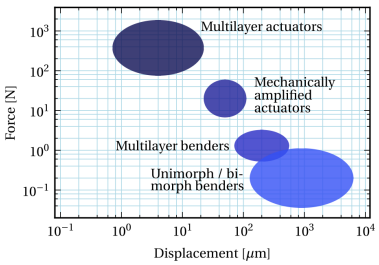

FIGURE 2.6: Transducers functioning fields[8]

Even though Eq.2.7 indicates that d_{33} mode obtains a significantly higher rate in strain-to-energy conversion rate, the high stiffness of the material requires much larger force to generate equivalent strain than the d_{31} mode. With the same force applied to both modes, the power output of piezoelectric materials with d_{33} mode is 2 orders lower in magnitude than the output of d_{31} mode. Thus, despite the d_{33} mode outperforming the d_{31} mode in high-force applications with its robustness and high efficiency, its stiffness does not favor vibration energy harvesting which required large displacement with

small force input[23]. On the other hand, d_{31} mode provides more acute sensitivity in response to vibration, specifically when designed into cantilever shape, the increase in compliance allowed even larger strains to be produced with smaller input forces[7], as shown in Fig.2.6. The use of benders is therefore to fulfill those conditions of vibration energy harvesting with low input forces and high required voltage output.

2.2.2 Benders and unimorphs

Benders are composed of thin, d_{31}, piezoelectric plates which are polarized in their thickness direction. The most widely used form of bender is the bimorph, consisting of two thin polarized piezoelectric plates bonded to a substrate by glue. As the plates are being actuated by the applied voltage, the material expands in the direction of the electric field, i.e. the thickness direction, and shrinks in the perpendicular directions, forcing the entire bimorph to bend as the substrate is not subject to this shape change, as shown in Fig.2.7, thus getting the name bender. While bimorphs generate higher energy density output, the high price for production and the deficient microfabrication technique limit its manufacturability and application for very small scales such as MEMS[24].

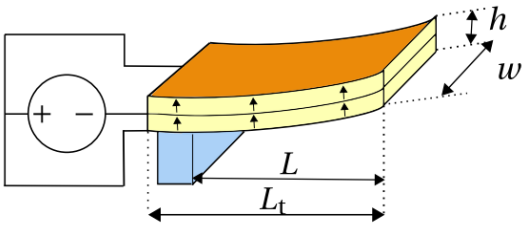

FIGURE 2.7: Basic illustration of a bimorph activated to bend[8]

Similarly, unimorphs (or monomorphs) are made of single piezoelectric plates glued to an inactive substrate material. Since bending produces tension and compression on the material simultaneously, leading to the electrical energy self-cancelled within the material, the piezoelectric plate is designed to be bonded with an elastic substrate, often metal or carbon fiber[12]. The difference in materials, indicating disparity in thermal expansion coefficients, often leads to thermal instability. In consequence, the application of unimorphs requires extra consideration of temperature.

2.2.3 Mathematical modelling

In order to improve the design of the transducers, proper models are needed for precise performance prediction. Vibration could be initiated by diverse factors, under which each system has unique characteristics. Nonetheless, those systems are able to be simplified to a single degree of freedom, lumped spring-mass system and described by two parameters, damping constant and natural frequency. As shown in Fig.2.8, a piezoelectric cantilever beam with a proof mass at the end and a multilayered piezoelectric plate could be simplified as an equivalent lumped spring mass

system. Arrows in Fig.2.8(a)(b) at the contact points are used to indicate the source of vibration, where $y[m]$ refers to the displacement of the base and $x[m]$ refers to the total displacement of the mass. The governing equation of motion for the lumped

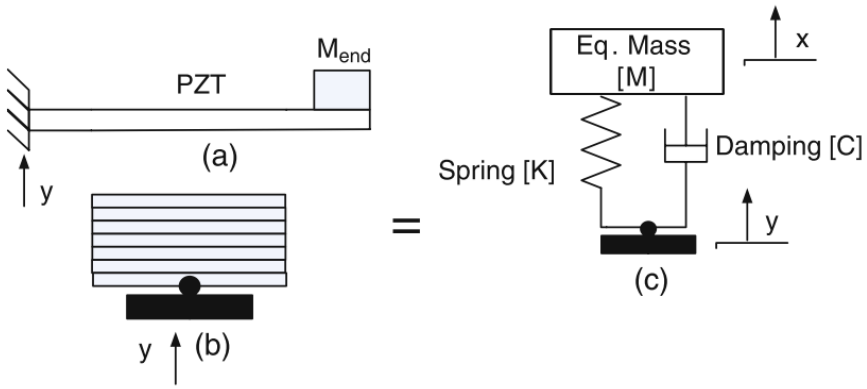

FIGURE 2.8: Equivalent lumped spring mass system of a vibrating rigid body[25]

spring mass system in Fig.2.8(c) could be obtained from D'Alembert's principle, written as:

$$m\ddot{z} + c\dot{z} + kz = -m\ddot{y} \tag{2.11}$$

in which m [kg] is the total mass of the system, c [Ns/m] is the damping of the system, k [kg/s^2] refers to the stiffness response to each loading condition, and z[m] denotes the net displacement of the mass, $z = x - y$.
The damping factor ζ is the ratio of system damping to critical damping, which is expressed as:

$$\zeta = \frac{c}{2\sqrt{mk}} \tag{2.12}$$

and the natural frequency ω_n is defined as:

$$\omega_n = \sqrt{\frac{k}{m}} \tag{2.13}$$

where the stiffness k [kg/s^2] was calculated by

$$k = \sqrt{\frac{3EI}{L^3}} \tag{2.14}$$

Noted that the average bending stiffness EI for the unimorph is[26]:

$$\overline{EI} = \frac{12}{w}\frac{E_p^2 t_p^4 + E_s^2 t_s^4 + E_p t_p E_s t_s (4t_p^2 + 6t_p t_s + 4t_s^2)}{E_p t_p + E_s t_s} \tag{2.15}$$

where E refers to the Young's modulus and t represents the thickness of the material. The ratio of output $z(t)$ and input $y(t)$ could be obtained by applying Laplace transform on Eq.2.11 with the expressions of damping constant ζ and natural frequency ω_n:

$$\left|\frac{Z(s)}{Y(s)}\right| = \frac{s^2}{s^2 + 2\zeta\omega_n s + \omega_n^2} \tag{2.16}$$

Assuming that the external base excitation is sinusoidal, $y = Ysin(\omega t)$, the time domain response of Eq.2.16 is:

$$z(t) = \frac{(\omega/\omega_n)^2}{\sqrt{(1-(\frac{\omega}{\omega_n})^2)^2 + (\frac{2\zeta\omega}{\omega_n})^2}} Ysin(\omega t - \phi) \tag{2.17}$$

in which the phase angle ϕ can be expressed as $\phi = arctan(\frac{c\omega}{k-\omega^2 m})$.
The approximate power generated from the piezoelectric transducer could be obtained from the product of velocity and force acting on the tip mass:

$$P(t) = \frac{m\zeta Y^2(\omega/\omega_n)^2\omega^3}{(1-(\omega/\omega_n)^2)^2 + 4\zeta^2(\omega/\omega_n)^2} \tag{2.18}$$

Power generated reaches the maximum as the operation frequency equal to the natural frequency:

$$P_{max} = \frac{mY^2\omega_n^3}{4\zeta} \tag{2.19}$$

Eq.2.19 indicates that energy output can be optimized by increasing the mass, excitation amplitude, and natural frequency, or reducing damping[22].

2.2.4 Mechanical performance improvement

Even though models have been developed to predict the behavior of benders, both results from experiment and models show that the performance of the benders alone is limited, especially as the needs of system move to smaller and smaller scale. In this case, the efficiency of power generation becomes more problematic and calls for improvement and optimization beyond what is expected for larger scale devices.

Research indicates that the conversion efficiency is closely related to the electromechanical coupling effect, damping effect, excitation frequency and electrical load[28]. While it has been shown that performances of the piezoelectric system can be improved as the mechanical damping is minimized [29][30][31], the lightly damped systems show the least bandwidth as they reach the peak power generation. Apart from the restriction caused by damping, the resonance frequency itself is generally too high for most energy sources, and the conversion efficiency greatly drops once the excitation frequency deviates from resonance frequency[32]. Fig.2.9 demonstrated the effect when the frequency of the base excitation drifted apart from the natural frequency. The power has fell to less than 1% of the original output within 5% deviation from the natural frequency. For most of the environmental sources, the frequency and magnitude of the vibration are non-regular, and how to effectively generate sufficient power among stochastic excitation is another problem to be considered. Research has been carried out to solve the above issues, aiming to improve the energy harvesting efficiency.

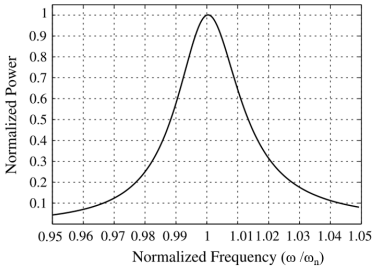

FIGURE 2.9: Power drop with the deviation of natural frequency[27]

It is common to put an inertial mass at the tip of the bender in order to lower down the resonant frequency of the system to match the energy source[33]. Jia and Seshia (2016)[34] discovered that larger tip mass would help yield better power responsiveness, specifically as it occupies approximately 60%-70% of the beam length. While the additional proof mass is proven to be able to lower down the natural frequency of the system, it also increases the size and weight to the system, as well as the probability of mechanical failure. Based on proof mass, more elaborate designs are to be developed.

Impulse excitation

Another widely investigated method focuses on impulse excitation, using the low frequency source vibration to excite the higher resonance frequency of the transducer. The first impaction frequency up-conversion adopted in energy harvesting was introduced by Umeda (1996)[35], who analyzed the efficiency of the energy transformation from the impact of the steel ball on the piezoelectric membrane. Gu et al. (2011)[36][37] suggested two rigid beams limiting the deformation of the bender at the same time impacted by bender and thereby achieves a high power density. Galchev et al. (2009 and 2012)[38][39] came up with impact driven package device that performed with high efficiency in the interested frequency range within small space requirement. On the other hand, Dhakar et al. (2013)[40] used a soft spring attached with a proof mass as an extension of the bimorph to achieve higher power output.
Unlike impact involves transfer of momentum, plucking involves the deformation and release of the piezoelectric harvester. From the moment of the release, the harvester would vibrate at its own natural frequency. This method is used when the driving frequency is much lower than the natural frequency of the system, especially cases like human body. Pozzi (2012)[41] presented the basic mathematic model for plucking and proved the promisingness of the technique. Pillatsch et al. (2014)[42] simulated the model and validated the feasibility of the model adoption. Kleiva et al. (2019)[43] used multi-magnet to yield several consecutive magnetic excitation per plucking cycle, which improved the power conversion.
Magnetic excitement is a non-contact approach researchers came up with. Tiek et al. (2006)[44] and Wickenheiser et al. (2010)[45] presented linear devices with magnetic actuation by inducing impulse with attraction of the bender and nearby ferromagnetic structure, allowing the bender to vibrate at its resonant frequency irrespective of the driving frequency.
In order to more precisely match the vibration energy, researchers also came up with systems with a combination of multiple harvesters under different natural frequencies that are able to perform in multiple modes. Malkin et al. (2005)[46] and Ferrari et al. (2008)[47] used piezoelectric beams with varying lengths, while Yang et al. (2009)[48] connected two benders with closed resonant frequencies with compliant material to widen the bandwidth.

Stiffness alternation

Stiffness is also a straightforward perspective to work on for the performance improvement. The coupling coefficient depends on the stiffness, and therefore studies on changing the transducer stiffness have been widely discussed in order to optimize the power conversion.
The most straightforward approach was presented by Lesieurtre et al. (1997)[49], who reduced the structure stiffness and thereby increased the coupling coefficient by applying a preload of half the buckling load to a symmetric piezoelectric bimorph. Leland et al. (2006)[50] further adopted the technique of applying axial pre-compression load to tune the natural frequency, while Morris et al. (2008)[51] applied tensile axial load to a tunable frequency mechanism.
Mann et al (2009)[52] introduced a device that adopted nonlinear stiffness response, pointing out the imprecise frequency matches of linear devices – even using multi-frequency excitation – which leads to underperform when applied in real cases. Stanton et al (2009)[53], based on Mann's idea, presented softening and hardening stiffness responses of the piezoelectric cantilever by changing the rectilinear position of external magnets.
Changing position of external magnets was also an approach to tune the resonant frequency of the system, broadening the bandwidth of the device. Challa et al.[54] first presented the technique of magnetic force tuning by changing the separation distances between magnets on the cantilever tip and magnets aligned vertically to the cantilever. On the other hand, Cottone et al. (2009)[55] invented a bimorph with a tip magnet as a pendulum repelled by another magnet at transversely changeable position while Zhou et al. (2013)[56] altered the magnetic force with rotatable external magnet. Al-Ashtari et al. (2012)[57] modified the previous designs using attraction forces, allowing manipulation of natural frequency during the operation.

Configuration optimization

Instead of focusing on the aforementioned methods which add extra force or objects to form systems, some researchers directly change the geometry, the form and thickness, of the benders to convert energy more effectively. Todd et al. (2006)[58] discovered that by reducing the thickness of the bimorph elastic layer can the resonance frequency of the system be reduced. However, the varied strain distribution in cantilever beam results in some parts of the material under fully utilized. Roundy et al. (2005)[59] claimed that trapezoidal configuration allows even distribution of the strain, while Baker et al. (2005)[23] and Yuan et al. (2008)[60] showed theoretically and experimentally that the triangular and trapezoidal cantilever beams have higher power output to the traditional rectangular ones.

2.2.5 Lifetime reliability

Plenty of research were done to improve the performance of the cantilever-type harvesters as they have shown considerable potential in vibration energy harvesting. As the studies focusing intensively on output improvement sprung up, some others started to pay attention to the reliability of the long term performance. Cain et al. (1999)[61] first suggested the detriment of cyclic mechanical stress to the degradation in piezoelectric material. Gall et al. (2007)[62] investigated the degradation behavior on the PZT wafer with 4-point-bending test, and showed that under 0.3% strain, the output charge declined 14% after 2000 cycles of operation. The work further presented the effect of the mechanical strain on the life cycle of the PZT unimorph, displayed in Fig.2.10(b), showing that the lower strain resulted in higher life cycle. Okayasu et al. (2010)[63] presented that the failure of the PZT cantilever comes mainly from the microcraks caused by mechanical strain, as displayed in 2.10(a), and Pillatsch et al. (2017)[64] further extended the cause of degradation to the recurrent condition forming microcracks in the tension layer. His work also pointed out that the region prone to break is where the material has the largest strain, which is the region near clamping area in the case of cantilever. Those microcracks may not necessarily lead to material breakage, but decrease the coupling factor and alter dynamic behavior instead.
Efforts have been made dedicating to minimize the strain without affecting the performance. Methods used could be roughly sorted into two types, the strain limiter and the compressive strain[65].

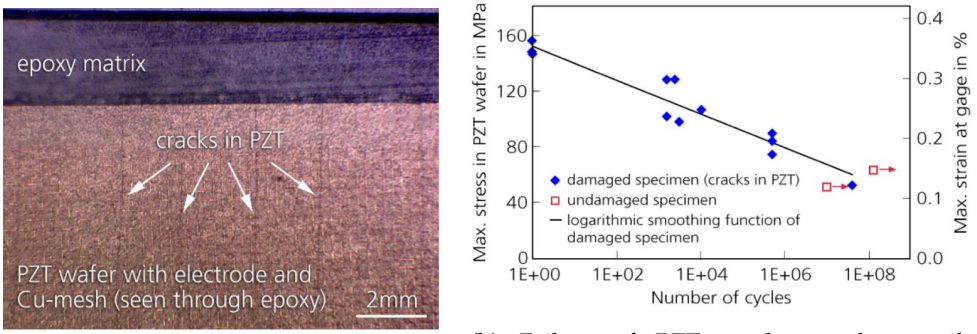

(a) microcracks in PZT layer[62]

(b) Failure of PZT patches under tensile loading[62]

FIGURE 2.10: Effect of mechanical strain on PZT cantilever

Strain limitation

Strain limitation ensures the motion of the cantilever is within the fracture limit, and is achieved by mechanical stopper that constraint the amplitude of the cantilever vibration. Singh et al. (2012)[66] was the first one to apply the stopper design into the tire energy harvesting device as a protection. The stopper was later developed as means of frequency-up system using impacts to trigger close-to-natural-frequency vibration[67]. Dakhar et al. (2013)[40][68][69] also found that stoppers created a broader bandwidth of the harvester by performing an increasing frequency sweep, as shown in Fig.2.11. Wang et al.(2019)[70] improved the frequency-up device and suggested that, within proper gap between bender and stopper, device with stoppers outperform the device with no stopper, as shown in Fig.2.12.

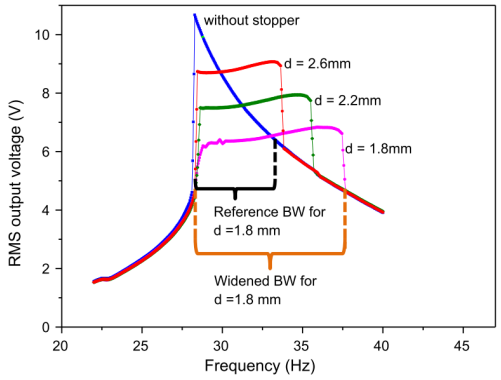

FIGURE 2.11: Bandwidth widening of device with different stopper gap d[40]

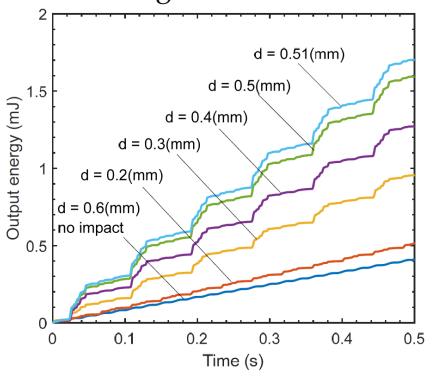

FIGURE 2.12: Steady-state energy output of the piezoelectric beam with different stopper gap d[70]

Compressive strain

As mentioned, most of the failures are caused by tension load, and this approach aims to keep the active layer at the compressive side to reduce the cracking generation. This method was done by pre-loading the piezoelectric layer, which was done by Mossi et al. (2003)[71]. Majer et al. (2018)[72] adopted a multi-layered design, and ensure the harvester under compressive stress by manipulated on the difference in thermal expansion coefficients.

Chapter 3

Experiment

The main objective of this research is to optimize the performance of a cantilever-type energy harvester in terms of energy output and lifetime with the employment of the limit stoppers. For the purpose of doing so, experiments conducted during this research were categorized into two parts in accordance with the domain of study, and harvesters under various conditions were tested in each domain. The variation of the sample includes the length, mass attached at the tip, and the configuration of the unimorph. The first set of experiments focused on the output aspect of the performance, comparing the influence of the stroke on power generation under different conditions. It began with the study of stroke-free vibration, followed by the analysis of the effect of the deflection constraint to the output by the mechanical stoppers. The second set of experiments focused on the performance with regard to the operational life. Experiments under all the aforementioned factors were conducted and analyzed in the view of lifetime. The conditions under each experiment carried out would be explained in the following sections, succeeding after the introduction of the sample fabrication, setup, and the preparatory experiments.

3.1 Design and Fabrication

3.1.1 Sample design

The unimorph was composed of two plates, a piezoelectric material as a harvester and an elastic substrate, a glue to bind the plates and a layer of electrode. The PZT5A4 was selected as piezoelectric material due to its high dielectric coefficient and electromechanical coupling factors, which allow a high signal-to-noise ratio and large deflection under load. The substrate attached was Pernifer 45, also known as alloy 45, whose thermal expansion coefficient is closed to the PZT5A4 to prevent delamination during heating. The two materials were bound by epoxy 302-3M blended with 5 wt% nickel balls which made the glue conductive. A thin layer of carbon paste, Dupont 7102, was coated on top of the PZT5A4 as an electrode. The properties of each material are shown in Table 3.1, noted that the thicknesses of the carbon paste and the epoxy was dependent on the fabrication process, and a schematic structure of the unimorph is shown in Fig.3.1.

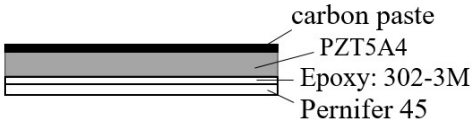

FIGURE 3.1: Schematic structure of the unimorph layer composition

TABLE 3.1: Sample materials and properties

	Young's Modulus	Material thickness
DuPont 7102	–	
PZT5A4	69 GPa	0.25 mm
302-3M	3.147 GPa	–
Pernifer45	193 GPa	0.1 mm

3.1.2 Sample fabrication process

The first step for fabrication of the unimorphs was to mix the epoxy to glue the two plates. The resin and the hardener were mixed together in the ratio of 100:45 by weight with stirring speed of 2500 rpm for 5 minutes by the speed mixer. Nickel balls were then added to the epoxy, in the ratio of 5% by weight, to induce the electrical conductivity and mixed with the stirring speed of 750 rpm for another 5 minutes until the complete dissolution of the mixture. After the glue was properly mixed, the next step was gluing the plates together. The PZT plate was lay on top of the substrate once the glue was spread on the substrate by the doctor blade. The two plates were then pressed tightly by a mass on top for 3 hours and put into the oven at 65°C to cure for an extra 3 hours. Lastly, carbon paste was spread on top of the PZT plate as the function of electrode, compacted and smoothed by doctor blade, and the sandwich structure was then placed in the oven at 120°C for 20 minutes to cure the carbon paste.
Afterwards, the plates were cut into the desired dimensions. In this research, all unimorphs were designed to had a width of 5 mm. Three different free lengths - 20, 30, 40 mm, were used, added with an extra length, roughly 3 mm, for clamping.
The tip mass located at the end side of the unimorph was composed of stacked pieces of steel foil, bound by 3M Scotch-Weld Super Glue. Each piece of the foil had the width of 6 mm and length of 3 mm, and two thicknesses of the foil, 0.1 and 0.25 mm, were used to more accurately meet the desired mass.

3.1.3 Contact poling

To induce the piezoelectric and pyroelectric activity of the PZT plate, a poling treatment was undergone to give an orientation of polarization by applying a high electric field of 500 V (2 kV/mm) to the PZT plate in the thickness direction for 5 minutes. In this study, two configurations of unimorphs were used, namely the straight and curved cantilever beams. The two types of unimorphs had nearly the same fabrication procedures except the order of the poling treatment. The PZT plate was poled before being bonded with the substrate in the case of straight unimorphs, while the curved unimorphs was poled at their final stage. As describes in the piezoeletric inverse effect, when an electric field is applied, the PZT would contract in the directions perpendicular to the poling direction. For unimorphs made to be curved, this

leads to inconsistent lengths of the two plates as the substrate did not respond to the applied voltage. For that the pernifer had already stuck to the PZT, the shortening in PZT pulls the pernifer to the side of the PZT, forming the curved configuration, as shown in Fig.3.2.

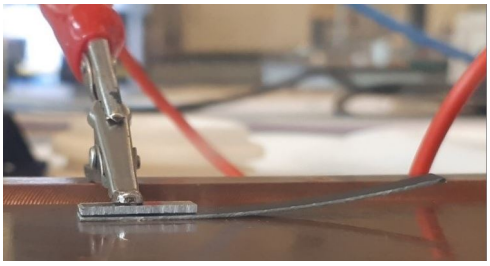

FIGURE 3.2: Curved unimorph poling

3.1.4 Stopper case design

For experiments under the condition of vibration with strokes, stoppers were needed to constrain the unimorph movement, as depicted in 3.3. In order to test the influences caused by the stopper at different distances, a stopper placed within the vibration frame was adopted to prevent errors in distance measurement. A case was designed to carry the unimorph along with the stopper over the vibration, at the same time allowing the stopper to switch the position easily. In the interest of a compact case design, the dynamic mechanical analysis and laser vibrometer were taken to study the properties and behaviors of the unimorph for determining the dimensions of the cases. The tests would be explained later in the preparatory section.

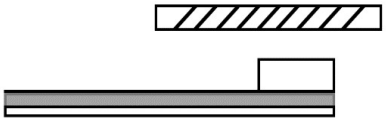

FIGURE 3.3: Concept of the stopper

Cases holding the unimorphs were designed slightly differently between the curved and the straight unimorphs. As shown in Fig.3.4, cases for straight unimorphs had a raised platform at the clamping area that allowed the unimorphs to bend downward. For the unimorphs that were pre-curved, which the equilibrium position had already been in the mid-air before starting the vibration, did not require an extra raising level of the clamp area. A bolt, located at the end side of the case and aimed to be hit by the tip mass, was used as the stopper and could control the distance between the unimorph through changing the height. Considering the size and the easiness in measurement, the ISO metric M3 bolts, which had the pitch of 0.5 mm, were selected.

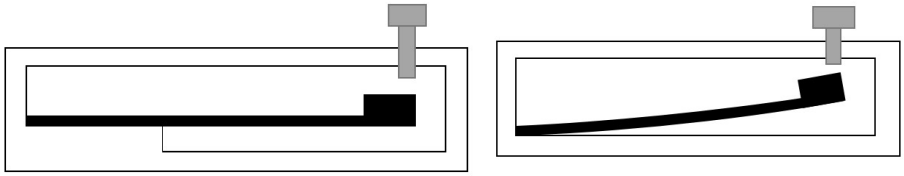

(a) case for straight unimorph (b) case for curved unimorph

FIGURE 3.4: Schematic figure for stopper case design

The dimension of the cases were determined by the vibration behaviors of the unimorphs. The inner height of the cases for the straight unimorphs were designed slightly larger than the total deflection range (two directions) of each length of unimorph added to the origin thickness of the unimorph and 300 mg tip mass. As for the curved unimorphs, since the configuration of the curved already occupied a certain extent of space, the heights of the cases were based on the displacement made during poling plus the deflection in response to the vibration.
The detailed dimensions of the cases design for different length of unimorphs are displayed in Fig.3.5. Parameters that change along with sample sizes are labeled in the figure and shown in the separate table 3.2.

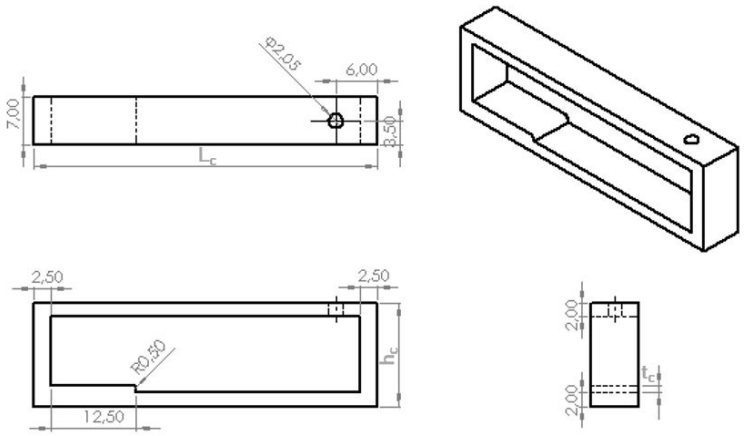

(a) Case for straight unimorphs

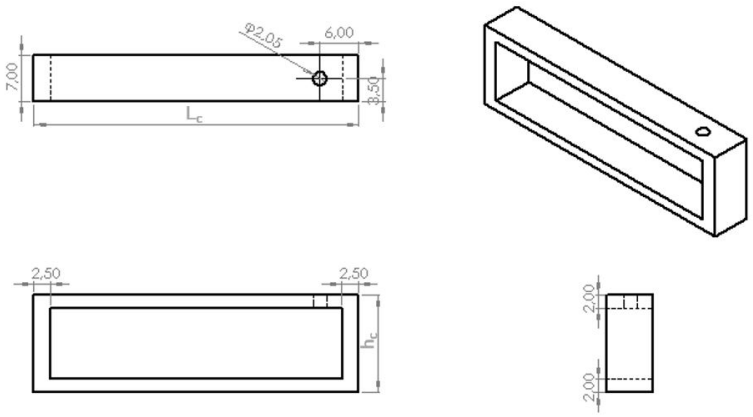

(b) Case for curved unimorphs

FIGURE 3.5: Dimension of the cases

TABLE 3.2: Parameters for case design (unit: mm)

	L_c	h_c	t_c
L20 unimorphs	40	12	1
L30 unimorphs	50	15	1
L40 unimorphs	60	15	1.5

The cases were made of acrylonitrile butadiene styrene (ABS) by 3D printing. Models of the cases were first designed and built in the software AutoCAD, and then printed at the smallest printer layer height, 0.06 mm, with 100% infill. After the support was removed, the cases were tapped to create thread for the bolts.

3.2 Experiment Setting

The following paragraph briefly introduces the entire equipment composition of this research. List of equipment is first presented, and the description of setting connection for vibration measurement and the logic of long term logging in the constructed software succeed.

3.2.1 List of equipment

Equipment used for signal measurement is listed as the following:

- function generator: Agilent 33210A
  The Agilent 33210A provides all types of primary waveforms, including sine, square, pulse, ramp, triangle, noise, and DC waveform, with the amplitude range from 10 mVpp to 10 Vpp and frequency up to the maximum of 10 MHz.
- power amplifier: Brüel&Kjær Type 2706
  The power amplifier Type 2706 increases the magnitude of power from an input signal to drive the vibration exciter, particularly the Brüel & Kjær Vibration Exciter Type 4809. The amplifier has a flat frequency response ($\pm$0.5 dB) from 10Hz to 20kHz, and the power output capability is 75 VA to a 3 Ω exciter with the maximum voltage gain 40 dB.
- shaker: Brüel & Kjær Vibration Exciter Type 4809
  Type 4809 shaker features a wide frequency range (10 Hz – 20 kHz) and a continuous displacement of 8 mm peak-to-peak.
- data acquisition chip: National Instrument USB-NI6008
  NI6008 provides 8 analog input channels, 2 analog output channels, 12 digital IO channels, and a USB port connecting to the computer. It is able to convert data up to the sampling rate of 10 k sample per second.
- oscilloscope: Agilent DSO-X 2004A
  The oscilloscope provides visualized signal and instant data analysis, including voltage peak-to-peak and voltage root-mean-square. Agilent DSO-X 2004A featured in 4 analog input channel, and a sampling rate of 2GS per second.
- accelerometer: Brüel & Kjær Type 4384
  Accelerometer converts the detected acceleration to voltage signals to display. Type 4384 accelerometer has a conversion rate of 0.817 mV/ms^{-2}, and is made specifically for vibration testing and analysis, as it features high sensitivity while low sensitivity to environment factors, and its service frequency range is 0.1 to 12600 Hz.

- dynamic mechanical analysis (DMA) tester: RSA G2
  DMA is a technique used to characterize the material's properties as a function of time, frequency, stress, or temperature. Various types of tests, including tension, shear, dual cantilever, three-point bending, to name but a few, were available for material with different geometries

- laser vibrometer: Polytec PSV-500
  The working principle of laser vibrometer is based on the Doppler effect, which describes frequency shifts caused by waves emitted from a moving source. The frequency shift, Δf, could be written as: $\Delta f = 2v/\lambda$, where v [m/s] is the velocity of the vibration object, and λ [m] is the wavelength.
  The vibrometer conducts a point-by-point measurement, directing a laser beam to a point on the surface of the vibrating object and measuring the frequency shifts from the reflected beam. The velocities of the points are then obtained from the formula, and their displacement could be derived from integration.

3.2.2 Measurement setup

Fig.3.6 illustrates the connection of the equipment used, and the setup for the main experiments could be divided into two parts: the part of mechanical vibration generation and that of electrical data measurement.
The mechanical vibration system comprised a function generator (Fig.3.6-1) generating continuous sine wave signals, an amplifier (Fig.3.6-2) magnifying the signals, and a shaker (Fig.3.6-3) clamping samples plus a accelerometer (Fig.3.6-4) as a reference to the measurement. Samples on the shaker were mechanically clamped by two metal plates with two screws. On the other hand, the electrical circuit part was composed of a variable resistor (Fig.3.6-5) to form a closed circuit for power measurement, shielded wire to block the electromagnetic interference, and oscilloscope (Fig.3.6-6) for instant signal measurement. Wires attached to the clamping plates had contact with the unimorph at the clamping area, and on the other sides connected to the shielded wire, which extended to the region where the other equipment was located and connected to the resistor box. The oscilloscope was connected in parallel with the resistor to measure the voltage output in the circuit. The data acquisition chip (Fig.3.6-7) had nearly the same function as the oscilloscope to measure voltage output, while it was specifically used for long term logging since it was more programmable yet had less sampling capacity.

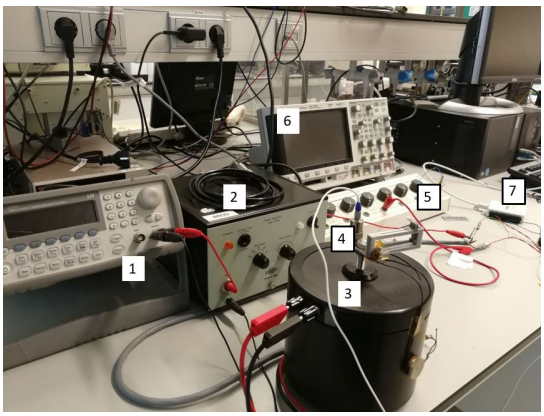

FIGURE 3.6: Vibration testing setup

3.2.3 General vibration condition

As the targeted working condition of this research was low frequency and high amplitude vibration at room temperature, a general vibration condition was determined for the succeeding measurement. Vibration at 40 Hz and 3.8 mm amplitude was the most reachable limit for the setup to meet the desired condition while remain under proper operation, i.e. generating stable, periodical low noise vibration from the shaker.

3.2.4 Lifetime experiments logging

In the long term lifetime experiment, data acquisition (DAQ) was used to periodically log the data. The program developed for the experiment had two forms of data logging, as presented in Fig.3.7. The program monitored the long term behavior by recording the average voltage peak-to-peak and voltage root-mean-square over half second every two minutes, and, meanwhile, logging the half-second waveform every five minute. Since, at the beginning stage of the crack formation, it could be observed by waveform but neither detectable in peak-to-peak nor root-mean-square value, recording waveform assisted in discovery breakage and analyzing the performance over time.

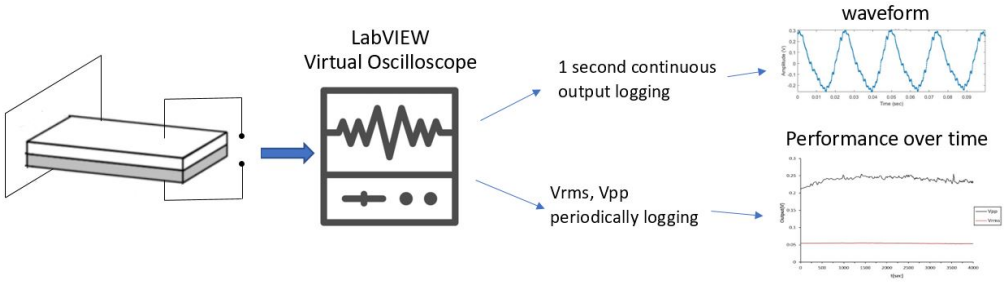

FIGURE 3.7: Schematic graph for the logging logarithm

3.3 Preparatory Experiments and Tests

3.3.1 Resistance matching

In order to measure the power output of the unimorph during the tests, a load resistance was essential, and an extra step for finding a proper resistance load was required to acquire the maximum output regarding the internal resistance of the unimorph that also consumed part of the power generated. As shown in Fig.3.8(a), a piezoelectric harvester could be described as the combination of a power source V_S, a capacitor C, and a resistor R_S.

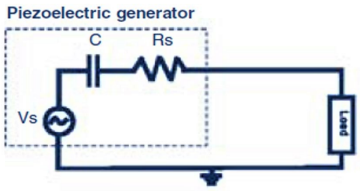

(a) internal circuit of unimorph[73]

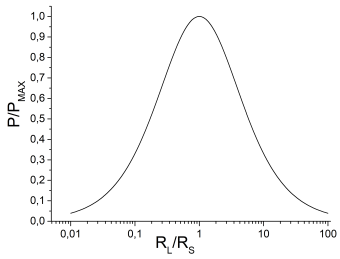

(b) Power variation in response to different load resistance

FIGURE 3.8: Resistance matching

The power provided by the source V_S would be split to both the internal load R_S and the external load, R_L proportion to their resistance ratio. The power received by the external load could therefore be obtained on behalf of the relation of the two loads.

$$V_R = V_S \times \frac{R_L}{R_S + R_L} \tag{3.1}$$

Where V_R denoted the voltage of the external load and the V_S was the voltage of the internal resistor. The power P_R, which was the product of the voltage V and current I, received by the load resistance was therefore:

$$P_R = I \times V_R = \frac{V_S}{R_S + R_L} \times V_S \frac{R_L}{R_S + R_L} = \frac{R_L}{(R_S + R_L)^2} V_S^2 \tag{3.2}$$

To obtain the maximum power generated, P_R was taken derivative with respect to R_L, where the extrema happened at $\frac{dP_R}{dR_L} = 0$:

$$\frac{dP_R}{dR_L} = V_S \times \frac{R_S^2 - R_L^2}{(R_S + R_L)^4} = 0 \tag{3.3}$$

Considering that the resistance are positive, only when the external load equaled to the internal load of the unimorph would the formula be fulfilled, allowing the output energy to reach the maximum. The relation of power received to the R_L is visualized in Fig.3.8(b), where the maximum output could be found at $\frac{R_L}{R_S} = 1$. For that the internal resistance of the unimorph was unknown, finding the ideal resistance required trial and error, and a variable resistor was used to help tuning to the matched load with the internal resistance. For every unimorph sample to be tested,

resistance matching would be done ahead of all the other measurement, and this step would not be brought up explicitly in the following experiments.

3.3.2 Failure strain measurement

All the vibration tests to be done in the following sections were based on the condition that the unimorphs vibrated in the safe regions that would not exceed their failure strain. In order to know the allowable deflection region, single cantilever test of the dynamic mechanical analysis (DMA) was applied to measure the bending strength of the unimorphs, and the results of the safe strain region would be the largest possible height for the box design.
Samples to be tested were unimorphs with length 20 mm and 40 mm, both straight and curved configuration. The unimorphs were tested under controlled strain rate at room temperature. As shown in Fig.3.9, the unimorph was clamped at one end while the other end was pushed by a loading nose with a cross-head downwards movement of 1μm/s.

FIGURE 3.9: DMA setup

3.3.3 Tip deflection measurement

Tip deflection measurement, on the other hand, was carried out to determine the smallest-acceptable height of the case design. Provided that the unimorphs would not exceed their strain limit during the given vibration condition, knowing the deflection of the unimorphs helped to design cases in proper sizes for the experiments. With the intention of measuring the tip deflection during vibration, the vibration environment was set the same as the general setting, which was 40 Hz and 3.8 mm amplitude at room temperature. Both straight and curved unimorphs were tested as well. Data of the identical length of unimorph with different tip mass were measured from the same unimorphs, which had the tip mass gradually added on top by 100 mg for each measurement.
A laser vibrometer was used to measure the deflection of the unimorph during the vibration, and the setup is shown in Fig.3.10. The scanning head was positioned parallel to the direction of vibration. Scanning points were assigned after the calibration of the software interface to the camera and determination of the coordination. Following, the measurement parameters, including the bandwidth, domain of measurement, would be decided. The measurement started once finishing all these settings. In this experiments, 21 points were assigned on the unimorphs, measuring 7 different positions over the length with 3 points in the same rows. Two extra reference points were assigned at the clamping area to extract the displacement from the base excitation. Each point was set to be measured 0.5 second at a sampling rate of 10,000/s.

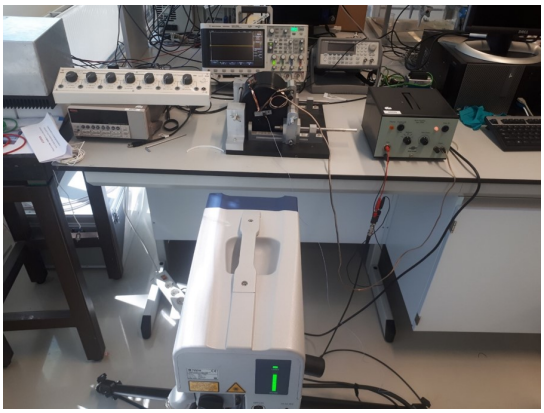

FIGURE 3.10: Laser vibrometer setup

3.3.4 Natural frequency measurement

In view of the considerable time length needed for measuring unimorph working lifetime in later experiments, accelerated method was adopted by increasing the excitation frequency. The only concern in speeding up was the frequency band affected by the natural frequency. As mentioned in section 2.2.4, when the unimorph vibrates close to the natural frequency, the vibration behavior turns fierce, at the same time creating plenty of extra motions. Aiming to keep away from this region, the natural frequencies and the scope of the influence were needed to be figured out to determine the accelerated frequency for the lifetime tests.
Since the measurement involved the condition close to natural frequency, the excitation amplitude was reduced to 0.2 mm during the test to avoid fracture happening. After matching with the load resistance, each sample started the vibration with 40 Hz and gradually added up by 20 Hz, the increase interval was adjustable depending on the adjacency to the natural frequency.

3.4 Exp 1 - Output Power Performance Analysis

The first experiment set studied the influence of limit stop on the power output of the unimorphs. General vibration tests without stoppers were first conducted at a set vibration condition while varying the attached mass and length of the unimorphs, and then the tests with stoppers involved followed.

3.4.1 Stroke-free vibration

For the vibration without strokes, the experiments performed here gave a general understanding of output performance of the unimorphs according to different configurations, lengths of sample and attached mass. Three different lengths of unimorphs – 20 mm, 30 mm, and 40 mm, and three different masses, 100, 200, and 300 mg, to be mounted, were chosen for testing (for convenience purpose, the rest of the report would use L20, L30, L40 and m0, m100, m200, m300 as notation). Considering that there existed discrepancies among samples, the same sample would be used for the tests under the same length in the interest of more conforming results.

A unimorph began tested with sole cantilever, and then 100 mg of mass was added on top of the unimorph tip each time after one round of measurement.

3.4.2 Vibration with strokes

The second part investigated the influence of the limit stop on power output. As known from section 2.2.5 that while limiting the deflection range of a cantilever prevents it from failure, the constraint also diminishes its output. In this section, a stopper was used to confine the deflection of the unimorph vibration. Changes in the distance between the stopper and the unimorphs were made so that the responding output power change could be analyzed.

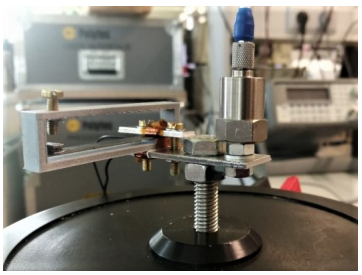

FIGURE 3.11: Case and stopper

In this set of test, the unimorphs performed vibration under the previous assigned vibration condition within the designed cases, and the bolt installed went downward closer to the unimorph with the decrement interval a quarter pitch, which was roughly 0.125 mm in height. The output root-mean-square voltage would be recorded before the bolt proceeded to the next position, and in the end all the output voltage would be converted into the power form according to the corresponding resistance of the unimorph. Fig.3.11 displays the case system of the experiment. A thin platform fixed to the shaker was carrying the entire case system, and another metal plate passing through the case clamped the unimorph together with the case at their base area. Here we give the definition to a term, h, which represents the distance between the stopper and the unimorph, as shown in Fig.3.12. The level of the top surface of the tip mass or the unimorph itself, if no tip mass was attached to, at static is defined as the origin, and the gap between the center line and the bottom end of the bolt was the value of h. The bolt come into contact with the unimorph when $h = 0$, and as it keeps on moving down, it starts to press the unimorph to bend below the original level, resulting in a negative value of h. During the experiment, the bolt started from the position of $h \approx 1.5$ mm and end at $h \approx -1$ mm, with some slight changes acceptable depending on the behavior of each sample.

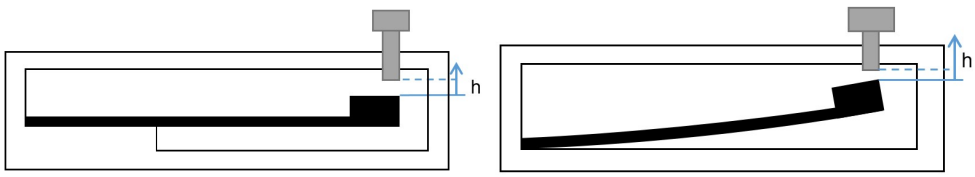

(a) h for straight unimorph (b) h for curved unimorph

FIGURE 3.12: Definition of stroke distance h

3.5 Exp 2 - Lifetime Performance Analysis

Conditions that allowed a larger output generation were discussed in the previous experiment set. Notwithstanding, the working lifetime is another notable aspect to be considered in terms of optimization, and the objective in experiment 2 is to study the performance in the view of operational life.
Seeing that it took longer time span for each lifetime experiment, approaches to promote the efficiency in progressing were adopted. Instead of taking all the previous conditions for testing, only one configuration of unimorphs were adopted as representative. Straight unimorphs at 40 mm was selected, as they were long enough to show characteristics of the unimorph vibration and provided enough range for stroke distance variation inspection plus their behaviors were more controllable and predicable than the curved unimorphs. On the other hand, to shorten the testing time for each sample, the tests were accelerated by adopting a slightly higher frequency, and the time span was limited to one day. For those experiments which duration longer than 1 day, the samples were directly regarded as having infinite lifetime. Experiments in this section were, likewise, separated into two by the presence of the limit stoppers during vibration.
As the length of the unimorph was fixed in this experiment set, testing vibration without stroke emphasizes on the effect of tip mass variation to lifespan. Random tip mass ranging from 200-320 mg were applied to the unimorph for testing, and ended up showing a tendency in lifetime variation along with the mass increment.
For the experiments of vibration with strokes, unimorphs were tested under different stopper distances with fixed tip mass 320 mg, as it was the largest mass in the previous test and was expected to have the fastest process. The stoppers started from $h = 0$ mm, with a increment of 0.25 mm, to $h = 1.25$ mm, where the position has already exceeded the range of vibration stroke.

Chapter 4

Result and Discussion

The previous chapter presented the methods employed to study this research topic. In this chapter, the hands-on laboratory results are investigated. The following content begins with a brief view on the effectiveness of the sample design and verification of the feasibility of the setup. The unimorph performances in each set of experiment are then discussed.

4.1 Design and Setup Evaluation

The evaluation of the experiment preparation focused on the structure of the sample and the reliability of the experiment setup. In the following, the efficacy of the sample with analytical perspective is discussed and compared with the real fabrication condition. Afterwards, the reliability of the setup is ensured in recognition of its consistent vibration environment and clear signals measurement.

4.1.1 Fabrication

Neutral axis calculation

As a means of guaranteeing that no self-cancellation happened in the piezoelectric material, calculations were made to find the position of the neutral axis.
The position of the neutral axis $\bar{y}$ could be expressed as:

$$\bar{y} = \frac{\Sigma E_i \bar{y}_i A_i}{\Sigma A_i} \tag{4.1}$$

where A_i referred to the cross section area, $\bar{y}_i$ was the position of the center line, and E_i denoted the elastic modulus of the specified material.
Since both the layer thickness and the elasticity of the carbon pasted were trivial, carbon paste layer was ignored in the following calculation. Terms definition are specified in Fig.4.1, where the width of the unimorph was given as w, and the thickness of the PZT, epoxy and substrate were t_0, t_1, and t_2, respectively. The top surface of the PZT was assigned to be the origin, and downward direction pointing to the other layers was in the direction of positive y (Fig.4.1).

Let $n_1 = \frac{E_{epoxy}}{E_{PZT}}$, $n_2 = \frac{E_{subs}}{E_{PZT}}$,
and the neutral axis therefore lies at:

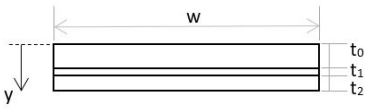

FIGURE 4.1: Terms of definition for unimorph layer composition

$$\begin{aligned}\bar{y} &= \frac{wt_0\frac{t_0}{2} + wn_1t_1(t_0 + \frac{t_1}{2}) + wn_2t_2(t_0 + t_1 + \frac{t_2}{2})}{w(t_0 + n_1t_1 + n_2t_2)} \\ &= \frac{t_0^2 + n_1t_1(2t_0 + t_1) + n_2t_2(2t_0 + 2t_1 + t_2)}{2(t_0 + n_1t_1 + n_2t_2)} \\ &= \frac{t_0^2E_{PZT} + t_1(2t_0 + t_1)E_{epoxy} + t_2(2t_0 + 2t_1 + t_2)E_{subs}}{2(t_0E_{PZT} + t_1E_{epoxy} + t_2E_{subs})}\end{aligned}$$

To ensure the PZT was kept under the same direction
of load, the neutral axis was required to stay below PZT, meaning that $\bar{y}$ had to be larger than t_0. The condition could therefore be expressed as:

$$\frac{t_0^2E_{PZT} + t_1(2t_0 + t_1)E_{epoxy} + t_2(2t_0 + 2t_1 + t_2)E_{subs}}{2(t_0E_{PZT} + t_1E_{epoxy} + t_2E_{subs})} \geq t_0$$

For the reason that the thicknesses of the two plates were both fixed, the thickness of t_1 was constrained to fulfill the desired neutral axis position:
$t_1 \geq \frac{-t_2E_{subs} + \sqrt{t_2^2E_{subs}^2 - E_{epoxy}(t_2^2E_{subs} - t_0^2E_{PZT})}}{E_{epoxy}}$
By substituting the symbols with the values of the material properties could one obtain the minimal acceptable thickness of epoxy, $t_1 \geq 0.0614$ mm.

Practical fabrication

Nonetheless, it was difficult to control the thickness of the epoxy glued between two plates in practical fabrication. The actual thickness of the epoxy that was made lay at the range between 0.04 to 0.06 mm, which were yet to reach the desired value. In other words, the neutral axis lay at the position between y= 0.238 and y=0.249 mm, which is smaller than 0.25 mm and still within the PZT layer. Under this case, around 0.002 to 0.024 mm thickness in the material did not generate usable energy and created inefficiency in energy output.

4.1.2 Setup reliability

There are a few aspects needed to be taken into account for a reliable setup – stability, repeatability, and signal clarity. Stability stands for offering the uniform, time-invariant vibration environment. Repeatability implies that variation of the testing results from the same sample would not occur under the same condition given. Signal clarity, same as the literal meaning, refers to recognizable and close to noise-free signals. Dedications were made to fulfill requirements from those aspects, and tests for verification are discussed in such order in the following paragraph.
The most direct metric for the stability evaluation was steady motion regardless of time variation within experiment or between the same experiments performed on different days. This could be validated through the measurement from the reference accelerometer. In Fig.4.2, an accelerometer recorded three acceleration of vibrations at the base platform over one day. Each measurement presents both its peak-to-peak voltage, V_{PP}, and root-mean-square voltage, V_{rms}, in the figure. It could be observed that the three signals were nearly identical, especially when the tests came to the later period, and remained constant over one-day length. Based on this outcome, the setup showed its stability through consistent motion regardless of time.

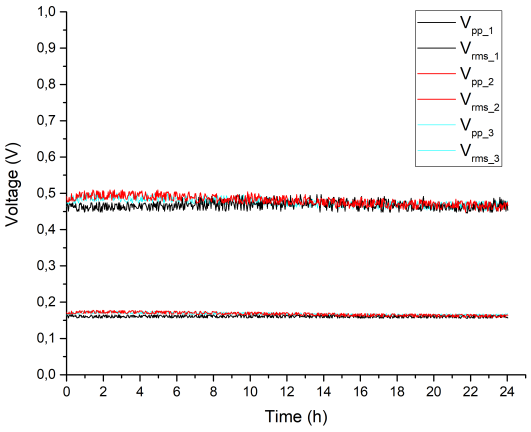

FIGURE 4.2: Vibration stability

Efforts made to improve the repeatability emphasized on minimizing the influence from human operation given that the requirement of the environment stability has already met. Among those steps involving hand operation, the mounting was the most influenced and inevitable process. Wires connection was deliberately designed to reduce the effects from moving the upper plate of the clamp during the sample installation and removal. Apart from that, the inconsistent clamping force has been the main concern of the mounting. As section 3.2.2 showed, the unimorph was clamped by plates tightened by two bolts. There was high possibility of the occurrence of uneven torques between bolts, or unequal force among different time of clamping. Since further control on clamping force was not attainable, tests were made to predict and understand the effects caused by different conditions of clamping. Considering that the clamping forces were too small to be quantified by the torque wrench, the clamping forces were roughly categorized into three levels: loose, medium, and tight, and the condition of uneven clamping in addition. The result (Fig.4.3) indicated that the clamping force barely affected on the output root-mean-square value.

Moreover, the output waveforms remained the same under different clamping condition (Fig.4.4). It could be inferred that, as long as the sample had proper contact with the circuit, the tightness and equity of clamping had little effect on the unimorph performance.

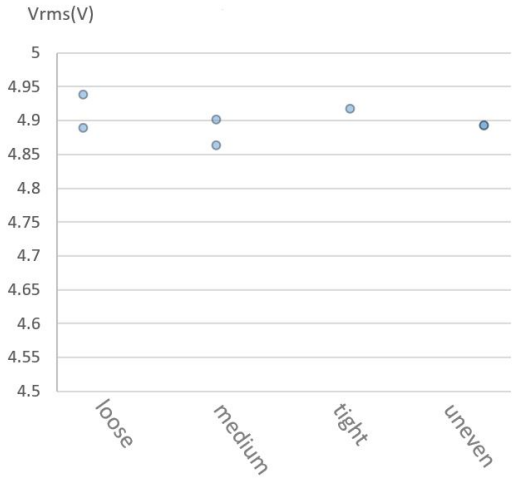

FIGURE 4.3: Clamping trial with various tightness

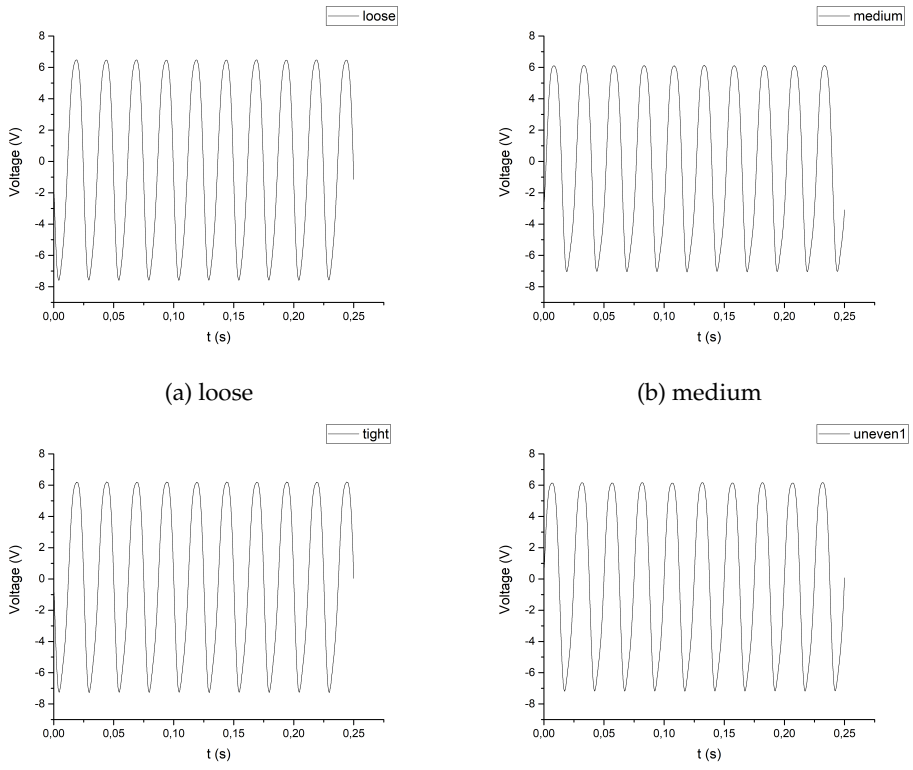

(a) loose

(b) medium

(c) tight

(d) uneven

FIGURE 4.4: Output waveforms for different levels of clamping tightness

Approaches taken to ensure signal clarity were preventing noise generation and blocking off the interference to the signal, i.e. the electromagnetic interference (EMI). Machines, especially the shaker in this research, had their own functioning bandwidth, and the output signals of the unimorph at different frequencies were tested. The compositions of the waveforms were analyzed through Fast Fourier Transform method to further understand the weight of the actual excitation out of the entire signal and noise. Fig.4.5 displays that the resonance or noise appeared more often at low frequency. Particularly at 30 Hz, the resonance frequency even dominated the signal output. The intervenes turned modest at 40 Hz, and the entire output signals were distinguishable and close to sine wave. This result confirmed that the previously determined 40 Hz was the lowest feasible frequency to be assigned as vibration condition. Also, the cases carrying the unimorphs and the stoppers were designed in thick walls to increase the rigidity so as to prevent extra vibration generated from the case during tests, which might physically intervene the normal vibration of the unimorph or signal-wise offer considerable noises to the output. The EMI was caused by physical contact and radiated induction, and in the setup of the research, not only from the circuit connection, but also the magnetic in the shaker itself contributed to the inference. Common ground connection and twisted as well as shielded wires adoption were used to isolate the noise.

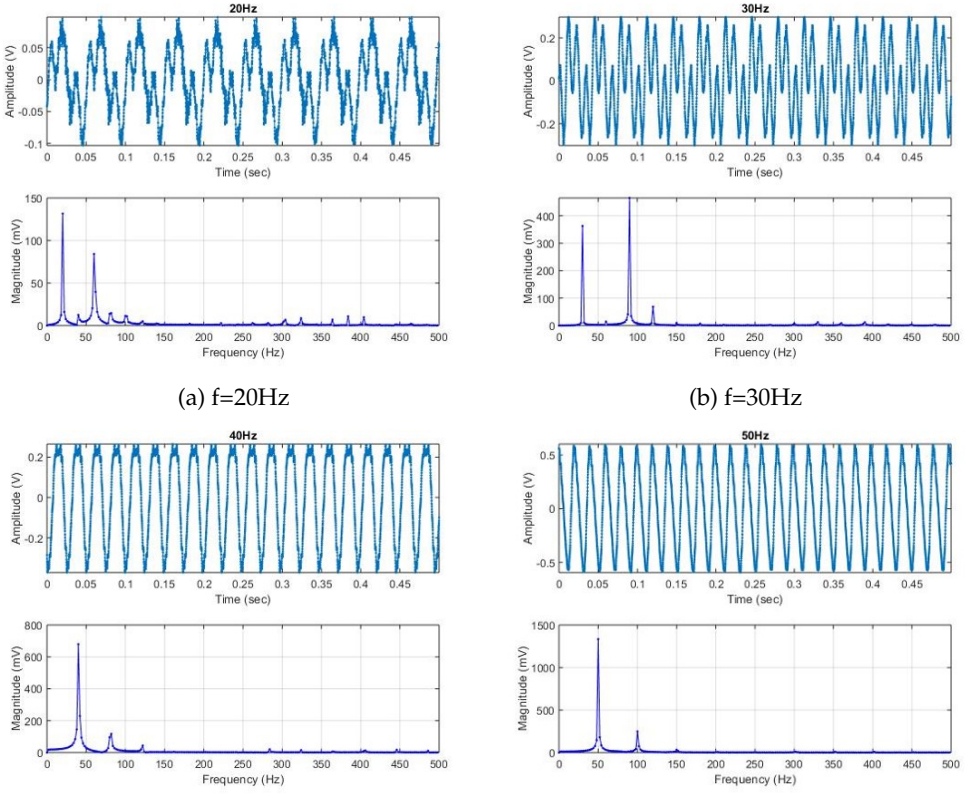

(a) f=20Hz (b) f=30Hz

(c) f=40Hz (d) f=50Hzn

FIGURE 4.5: Output waveforms analysis at different frequencies

4.1.3 Stopper material selection

On account of the inbuilt magnet of the electrodynamic shaker, a large magnetic field was formed, magnetizing the steel bolts which played the role of the stoppers constraining the deflection. Note that the substrates of the unimorph were also made of steel, the unimorphs were thus attracted and stuck to the bolt once the bolt was too close to the unimorph. To solve this issue, the bolt was switched to a non-ferromagnetic material, brass. Fig.4.6 compares the effect of the magnetic attraction by displaying the output with different stopper materials. The symbol h in the figure denotes the distance between the stopper and the unimorph. With the brass bolt, the impact of the bolt and unimorph started at the distance between 0.1 and 0.2 mm, where the output root-mean-square voltage value began to drop. However, the output with steel bolt had already declined when the distance between the two were larger than 1 mm, long before the start of the stroke vibration. This phenomenon was also observable in the experiment that the unimorph directly stuck to the bolt instead of moving back-and-forth. Therefore, instead of conventional steel bolts, brass bolts were adopted as the limit stoppers.

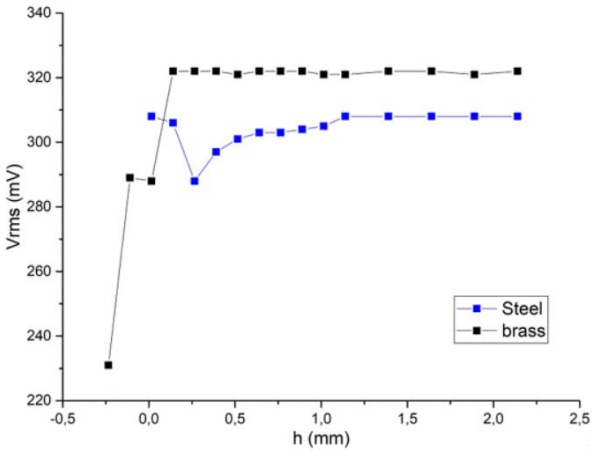

FIGURE 4.6: Comparison of the effect of a magnetized bolt placement on output change

4.2 Preparatory Experiments and Tests

4.2.1 Failure strain measurement

Several DMA tests have been carried out to measure the failure strain of the unimorphs, but a few terms needed to be defined in advance to the discussion. In our design of the unimorph, the PZT plate was set to place on the upper side. The zero line of the y axis laid at the top of the PZT, as shown in Fig.4.7. The direction of bending towards the PZT side was defined as positive, while towards the substrate was negative. As the unimorph bent upward, the PZT layer was under the state of compression whereas the substrate was under tension, and the opposite when it bent downward to the negative direction. The data measured was the displacement of the cantilever tip.

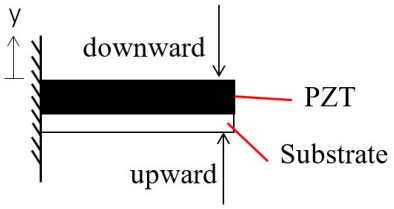

FIGURE 4.7: DMA axis definition

The results of the tests are shown in Fig.4.8. Same configuration or sizes were tested with several samples, and were labeled with numbers added at the legend. Samples with the same shape but tested under different directions are put in the same graph, and each graph displays the strengths in two direction of the unimorphs at that specific shape.

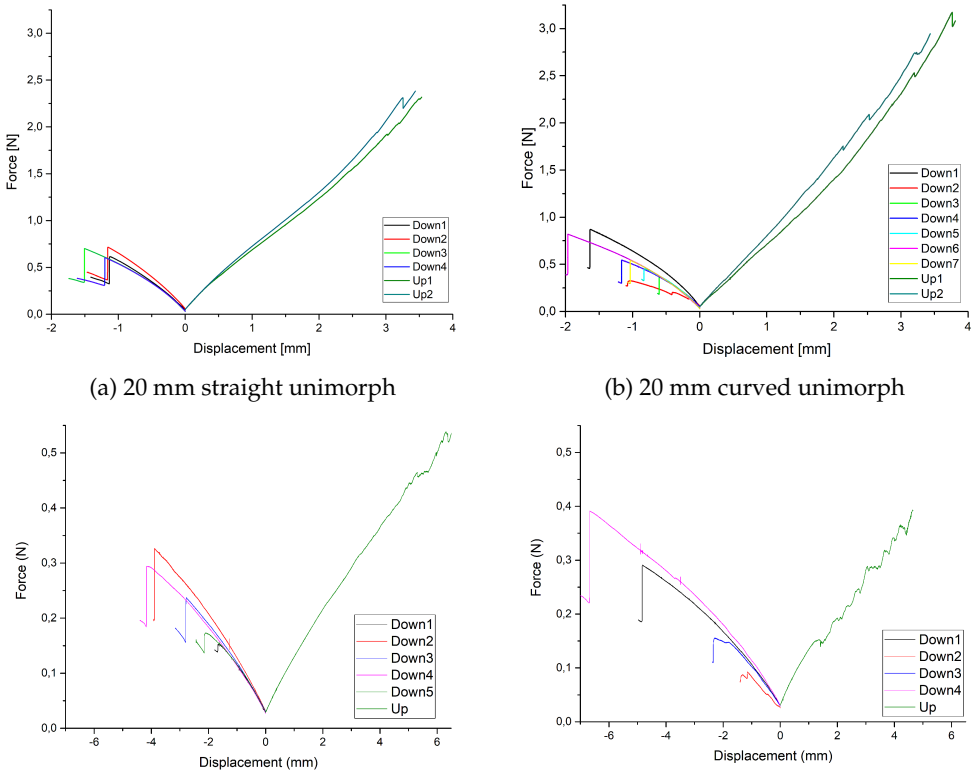

(a) 20 mm straight unimorph

(b) 20 mm curved unimorph

(c) 40 mm straight unimorph

(d) 40 mm curved unimorph

FIGURE 4.8: Failure strain tested by DMA

The slopes in the figures represent the relation between the force required for the corresponding displacement, which could be perceived as stiffness. From analytical aspect, according to Eq.2.14, $k_{eff} = \sqrt{3EI/L^3}$, the stiffness of the unimorphs decreased along with the increase in unimorph length. The experimental results conformed with it, as the average slope of the 20 mm straight unimorphs was roughly 0.6 [N/mm] while that of the 40 mm unimorph was 0.1 [N/mm]. Another finding was that, the strengths in upward direction were larger than the downward in each configuration. Since the PZT was the most brittle among all the materials in the unimorph, it turned out to be the determinant of the strength and the safe deflection range of the unimorph. Therefore, results showing higher strength in upward direction were expected, as ceramics better withstand compression than tension. Furthermore, straight unimorphs performed with a higher consistency than the curved ones during the measurement, and the longer the curved unimorphs were, the lower their performance consistency. In Fig.4.8(d), curved unimorphs performed greater differences in both failure strength and slope in the tests, especially for length 40 mm unimorphs. This could be inferred from the involvement of great amount of internal stress at formation of the curved configuration, which led to lower stability and greater divergence among samples. Considering that larger samples prone to magnify the inhomogeneity either inborn in materials themselves or formed during fabrication process, plus the aforementioned effect, all contributed to less controllable behaviors and the greater difference among failure strengths of the 40 mm curved unimorphs shown in Fig.4.8(d).

However, even though the curved unimorphs had less distinguishable strength and slope shown in the plot, it could still be concluded that, under the same deflection direction, the slopes of straight and curved unimorphs at the same length were nearly equal. Therefore, the behaviors of straight and curved unimorphs in response to subjected bending force were considered the same. Moreover, the safe deflection range for case design could be roughly determined - for the length 20 mm unimorphs were roughly within 1 mm downward to 3 mm upward while for the length 40 mm unimorphs were between 2 mm downward and 4 mm upward.

4.2.2 Unimorph tip deflection

Analytical solution

Analytical values of the tip deflection, d, along with different unimorph length were first derived from the equation of uniform cantilever with a tip mass.
Under the harmonic base excitation with the applied force $f(x,t) = F(x)cos\omega t$, the steady-state response $\omega(x,t)$ for the cantilever could be expressed as

$$\omega(x,t) = \sum_{r=1}^{\infty} \frac{\phi_r(x)}{\omega_r^2 - \omega^2} F_r cos\omega t \tag{4.2}$$

where x was the axis along the unimorph length direction, t indicated the time, ω referred to source frequency, r denoted the r^{th} vibration mode, ω_r indicated the corresponding natural frequency of the r^{th} mode of the uninorph, ϕ was the spatial

function of the movement, and

$$\omega_r = \lambda_r^2 \sqrt{\frac{EI}{mL^4}} \tag{4.3}$$

where the $= \lambda_r$ referred to the eigenvalue of the r^{th} mode. Under the condition of low frequency vibration, it was assumed that the unimorphs were performing the first mode of vibration alone, and the eigenvalues from each unimorph length and tip mass weight are listed in Table 4.1.

TABLE 4.1: Eigenvalue calculated according to different length and tip mass

length\mass	100 mg	200 mg	300 mg
20 mm	1.5006	1.3352	1.2332
30 mm	1.5855	1.4343	1.3352
40 mm	1.6384	1.5006	1.4060

Input the vibration parameters and the previous calculated eigenvalue to the equation, the tip deflections under each condition could be obtained, and the results were listed in the table below (table 4.2). The maximum deflection, which was expected to happen at length 40 mm unimorph with 300 mg tip mass, lay at around 1.2 to 1.5 mm of transverse displacement.

TABLE 4.2: Analytical deflection of the unimorph tip (unit: mm)

length\mass	100 mg	200 mg	300 mg
20 mm	0.0457	0.0746	0.1022
30 mm	0.2879	0.4538	0.6273
40 mm	0.5928	0.9418	1.3593

Experiment results

The experiment data collected were processed and the final tip deflection amplitude were shown in Table 4.3, and further plotted in Fig.4.9. The result indicated that the straight unimorphs, in general, had slightly larger tip deflections during vibration than the curved ones.

TABLE 4.3: Deflection measured by laser vibrometer (unit: mm)

	Straight Unimorph			Curved Unimorph		
	L20	L30	L40	L20	L30	L40
m0	0.0312	0.1591	0.4655	0.0261	0.1169	0.4510
m100	0.0484	0.1927	0.5966	0.0445	0.2004	0.5654
m200	0.0940	0.2381	0.7121	0.0627	0.2834	0.7045
m300	0.1201	0.3782	0.9681	0.1095	0.3561	0.8878

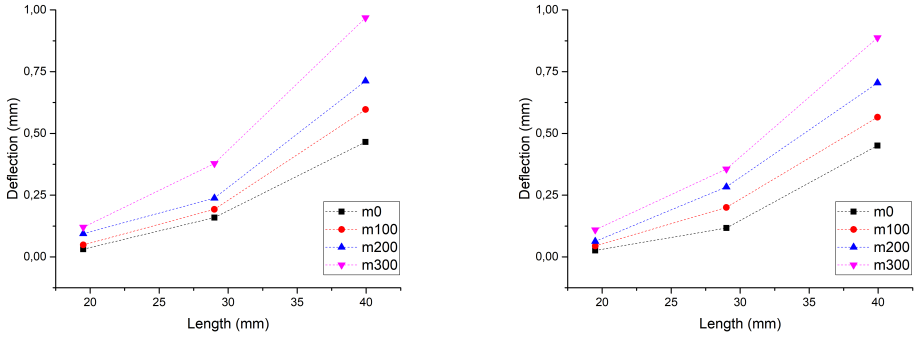

(a) straight unimorph (b) curved unimorph

FIGURE 4.9: Empirical unimorph tip deflection

Despite the fact that the largest deflection from the experiments was smaller than the prediction from the analytical model, comparing to the expected value derived in the previous section (Fig.4.10(a)), it could be observed that experimental deflections were larger than the analytical results when the unimorphs were smaller in either length or tip mass. Also, experimental results behaved in a different trend from the analytical curved trend. Upon discovering this, the plot was taken logarithmatically at both axis, the length and the deflection, to study the relation of the measured data and understand the difference between experimental and analytical values in trend (Fig.4.10(b)). The slope for each trend line denoted the exponent relation of the resulted deflection to the unimorph length. Analytical values obtained steeper slopes, which were in average 4.2, indicating that $d \propto L^{4.2}$, than the slopes from empirical data of the straight and curved unimorphs, which were in average 3 and 3.3, also known as $d \propto L^3$ and $d \propto L^{3.3}$, respectively. This explained the reason why the deflection of the theoretical value gained faster, as the relation of the analytical value was one order larger in exponent.

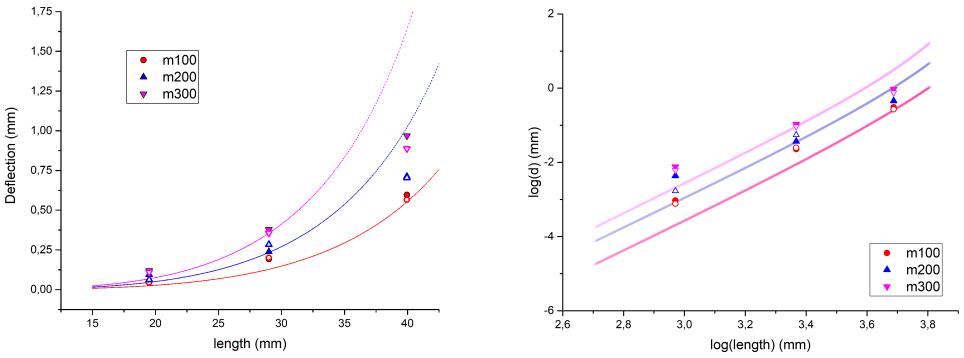

(a) Unimorph tip deflection (b) Logarithm of unimorph tip deflection

FIGURE 4.10: Unimorph tip deflection under different beam lengths, with the filled dots representing straight unimorphs experimental data, hollow dots the curved unimorphs, black dash lines the trend lines of the dots, and the dot line the analytical value of the deflection

Besides all the possible human factors during the measurement, including but not limited to inconsistent and uneven clamping force to the unimorphs, errors in measurement and errors accumulation in calculation, the deviation of the trends in experimental value from analytical value could be resulted from the over-simplified model. First, the unimorphs were not homogeneous over the length in thickness and epoxy distribution as assumed in the model. Another reason was that the model is valid for undamped vibration, while, in real life, it is difficult to create a damp-free vibration environment. Still another point worth mentioning is the idealized force condition adoption that contributes to deflection overestimation. The force applied in the model was assumed to be uniformly distributed in the entire beam, while the load applied to the unimorphs was varying along the beam length. The deflection derived from the varying distribution load has shown to be smaller than that from the uniformly distributed load[74], widening the gap between the analytical and empirical values. Moreover, the unimorph might include not only transverse bending in the movement. The non-uniformity allowed the generation of torsion and other movements, obstructing the cantilever to move smoothly in transverse direction and contributing to the deviation in deflection from theoretical results. In addition, it was discovered that factors influencing vibration behaviors are more sophisticated than mechanical issues – the load resistance was found to change the vibration amplitude as well[75]. This makes the deflection of the unimorphs less predictable.
The results of this experiment have shown that the maximum deflection under the given vibration condition was far less than failure strain measured in previous experiment, confirming our presumption of safe-vibration.

4.2.3 Natural frequency

The natural frequency variation of the unimorph as a function of free length and tip mass was investigated, and the results of the measurement are shown in Table 4.4. It could be observed that, the increase in either the unimorph length or tip mass effectively reduces the natural frequency. The power output at different excitation frequencies of unimorphs are shown in Fig.4.11 for much detailed depiction. It illustrates that increasing the tip mass attached not only reduces the natural frequency but also effectively increases the power output. Another noteworthy point is that the curved unimorphs obtain higher natural frequencies and larger peak values than the straight unimorphs at longer lengths. This could give the credit to the higher stiffness of the curved unimorphs resulted from the surface stress induced to maintain the curvature of the configuration[76].

TABLE 4.4: Natural frequencies of the unimorphs (unit: Hz)

	Straight Unimorph			Curved Unimorph		
mass\ length	L20	L30	L40	L20	L30	L40
0 mg	499	224	–	458	224	133
100 mg	341	167	102	287	172	105
200 mg	272	134	86	244	138	96
300 mg	235	111	78	228	125	87

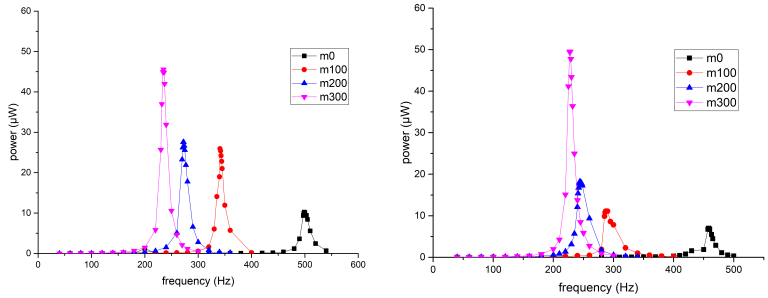

(a) L20 straight unimorphs (b) L20 curved unimorphs

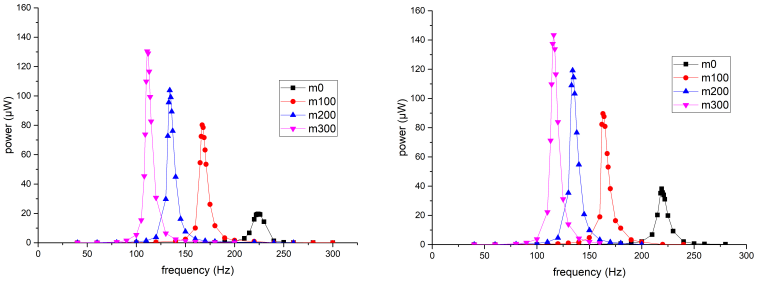

(c) L30 straight unimorphs (d) L30 curved unimorphs

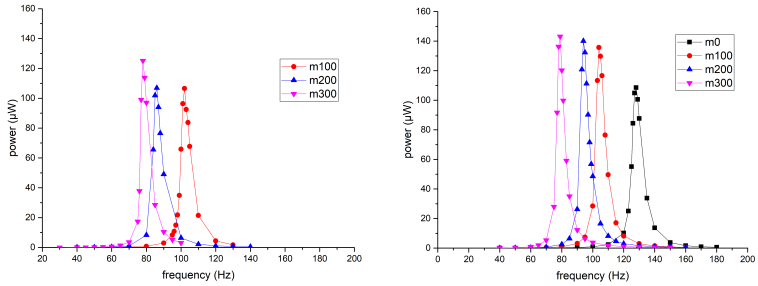

(e) L40 straight unimorphs (f) L40 curved unimorphs

FIGURE 4.11: Natural frequency of unimorphs

Comparing the experimental results with the analytical values, as shown in Fig.4.12(a), one could find that there are large deviations from the analytical values, especially from the two distinct rising trend. To further understand the relation between the unimorph length and the natural frequency, the figure was taken logarithm at both axes, as shown in Fig.4.12(b). The slope values in the graph presented the analytical relationship of $f_n \propto L^{-1.67}$ and the empirical relationship of $f_n \propto L^{-1.45}$, where f_n represented the natural frequency.

While, same as the previous discussion on large difference between empirical and analytical trends, the cause mainly came from the negligence of damping factors and oversimplified models, factors altering the natural frequency also included the clamping system. There existed another resonance for the entire clamping system, including the two plates and the cases, which might shift the maximum output of the unimorph from its own natural frequency. As the values measured were the results of the intervention by the environment system, they were possibly deviating from the analytical values.

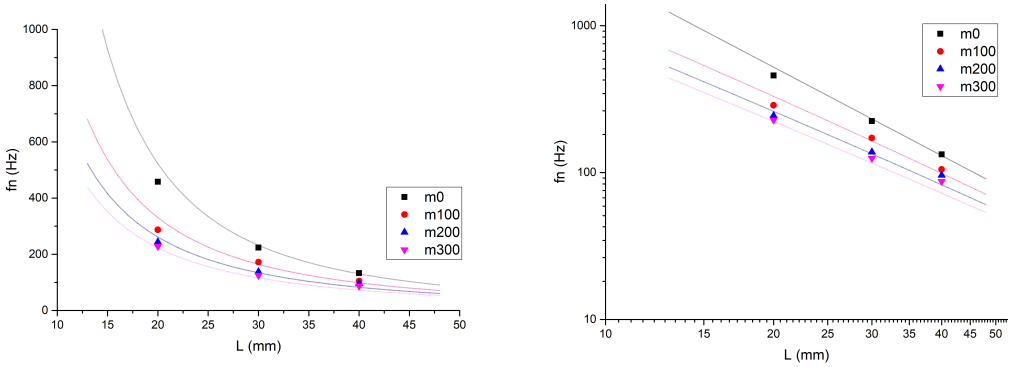

(a) unimorph natural frequency (b) Logarithm of unimorph natural frequency

FIGURE 4.12: Analytical and empirical natural frequency

The measurement results showed that (Fig.4.11(b)), the lowest natural frequency happened at 40 mm length straight unimorph with 300 mg tip mass, which was 78 Hz. Look further into the plot could one discover that the rise of the output peak initiated at about 60 Hz, and, to studiously avoid the rising peak, 50 Hz was selected as the accelerated vibration frequency for the long term test.

4.3 Ex1 - Output Power Performance Analysis

This section discusses the outcome of the first set of experiments. The expected output from the analytical model is first presented, followed by the comparison and analysis with output power measured from the stroke-free vibration. The results of vibration with strokes are then presented, and the discussion on the effects brought by the limit stops and possible benefits followed.

4.3.1 Power output vs. unimorph length

In advance to practical experiments, theoretical values for the straight unimorphs were taken as reference to predict the actual output. From the formula presented in section 2.2.3, the ideal output value could be calculated from Eq.2.18:

$$P(t) = \frac{m\zeta Y^2(\omega/\omega_n)^2\omega^3}{(1-(\omega/\omega_n)^2)^2 + 4\zeta^2(\omega/\omega_n)^2}$$

Practical experiments were carried out, and the measured output of the unimorphs are shown in Table 4.5 and Fig.4.13. Both the increase in tip mass and unimorph length contributed to the increase in power output. Besides that, a few remarks could be observed here. First, the performance of the straight and the curved unimorphs were comparable under the same operation conditions. The two configurations showed little difference in performance in terms of output. Next, the outcome of the experiment met the expected relation tendency. However, apart from the positive correlation, the values of the experiment results were much lower than the analytical values.

TABLE 4.5: Power output of unimorphs (unit: μW)

	Straight Unimorph			Curved Unimorph		
	L20	L30	L40	L20	L30	L40
m0	0.1616	1.1364	–	0.1667	1.8293	14.3990
m100	0.4462	3.4196	22.4720	0.4530	5.5543	24.7086
m200	1.1151	9.3571	41.2632	1.0323	12.8076	38.6142
m300	2.3452	23.6498	82.8016	1.9300	35.7505	88.2880

In order to further understand the trend of output increment along with unimorph length, both sides of the axis were taken logarithm, as shown in Fig.4.14. Same with the previous, the slopes of the trend lines indicate the power relation of the length to the output. The empirical data showed an average slope of 5.2, indicating that the relation between the two parameters in empirical result was $P \propto L^{5.2}$, which was milder than the analytical average of 5.6, meaning that $P \propto L^{5.6}$. The difference in the exponent contributed to the output deviation when coming to longer length of unimorphs.

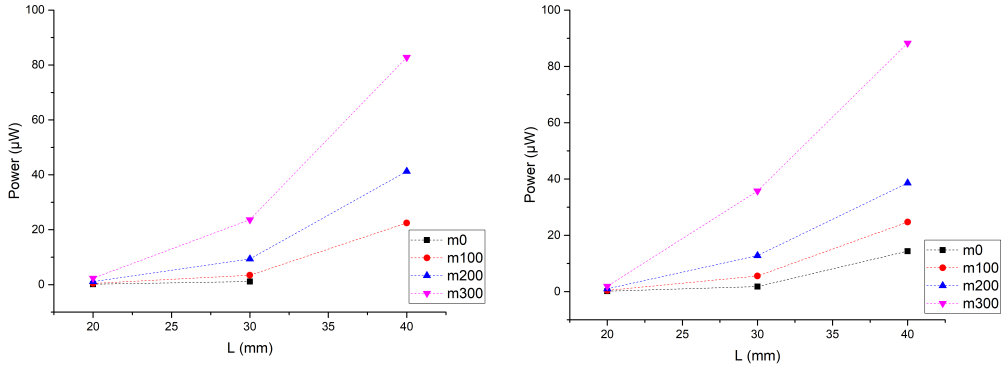

(a) straight unimorph (b) curved unimorph

FIGURE 4.13: Power output versus unimorph length

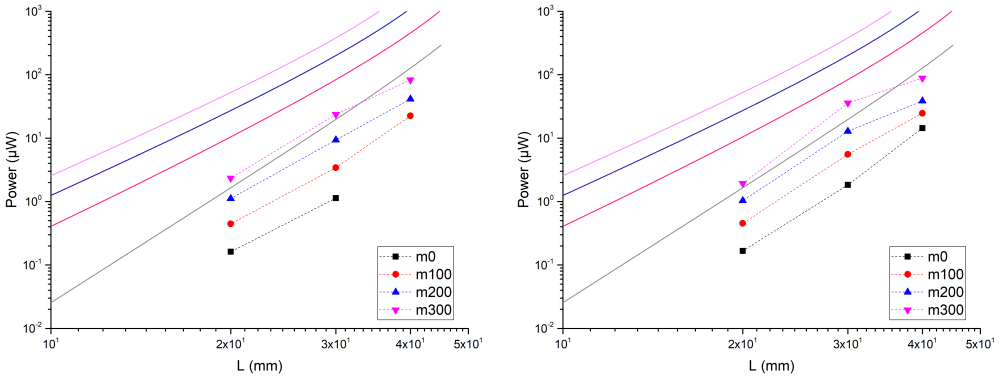

(a) straight unimorph (b) curved unimorph

FIGURE 4.14: Polynomial relationship of output and unimorph length

Looking into the large gap between the analytical and experimental value, possible explanations to the phenomenon are the oversimplified output model and the position of the neutral axis. The model used, in general, neglected the interacts or effects caused by the environments while the experiment setup did not allow to prevent those factors, such as air damping or heat generation during vibration, reasonable energy loss was expected. Another worth noticing is, as mentioned in section 4.1.1, the neutral axis of the unimorph from the actual fabrication lay in the PZT layer, leading to self-cancellation of a portion of power generated and a lower total output of the harvester. Furthermore, similar to the aforementioned issue, electrical factors influence the mechanical behavior of vibration as well, increasing the uncertainty in the unimorph performance, which also contributes to the gap between the expected and measured results.

4.3.2 Power output vs stopper distance

The measurement in this section was based on the results from the previous but with the involvement of the limit stops. A general scheme of output variation in response to stopper distance change is illustrated in Fig.4.15, in which is represented by a length 40 mm unimorph with tip mass 200 mg. The filled dots are vibration without the effect of the stoppers, dots with crosses indicates the conditions that impacts occur during vibration, and the hollow dots refer to the condition unimorphs are directly pressed by the stoppers. Under stroke-free vibration, the power generated maintains at the same output level. As the distance h continues decreasing, the unimorph starts to strike the stopper, which happens at $h = 0.5$ mm in the figure. The output power increases for a short while as the stopper distance keeps reducing, and then starts to fall sharply all the way through the condition when stopper directly presses the unimorph, which was when $h < 0$. If keeps pushing the stopper downward, the output value would reach another balance, where small, smooth output generated.

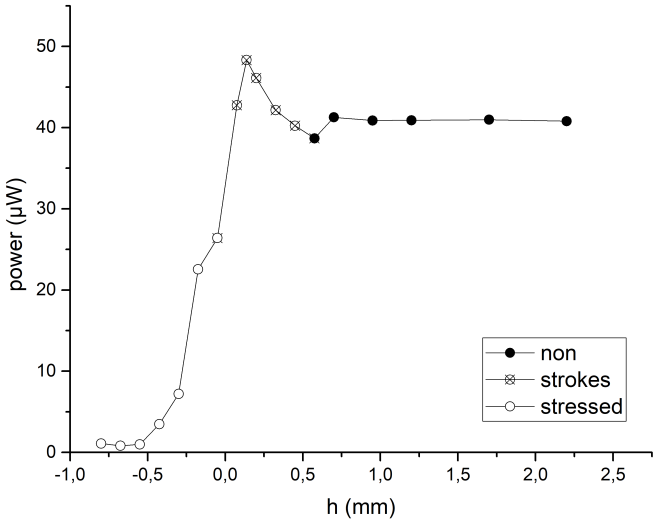

FIGURE 4.15: Concept scheme of L40 unimorph output versus stopper distance

The results for the measurement are shown in Fig.4.16. In the same way, hollow dots in the figures represents the vibration with strokes. Overall, there was no distinct output difference between the straight and curved unimorphs. Most of the sample followed the general relation displayed in Fig.4.15, and such distance relation between the bolts and the unimorphs could be roughly classified into three categories: no effect, impact, and pre-stressed. No effect, literally, refers to the condition that the position of the bolt was beyond the unimorph deflection range, and the output power in this category remained the same regardless of the h value. The relation is classified as impact when the bolt moved to the position where it would be struck by unimorph during vibration. The stage of pre-stressed described the condition in which the h was negative, and the unimorph was subjected to a downward load from the bolt. At this stage, the output power dropped significantly along with the reduction in gap.

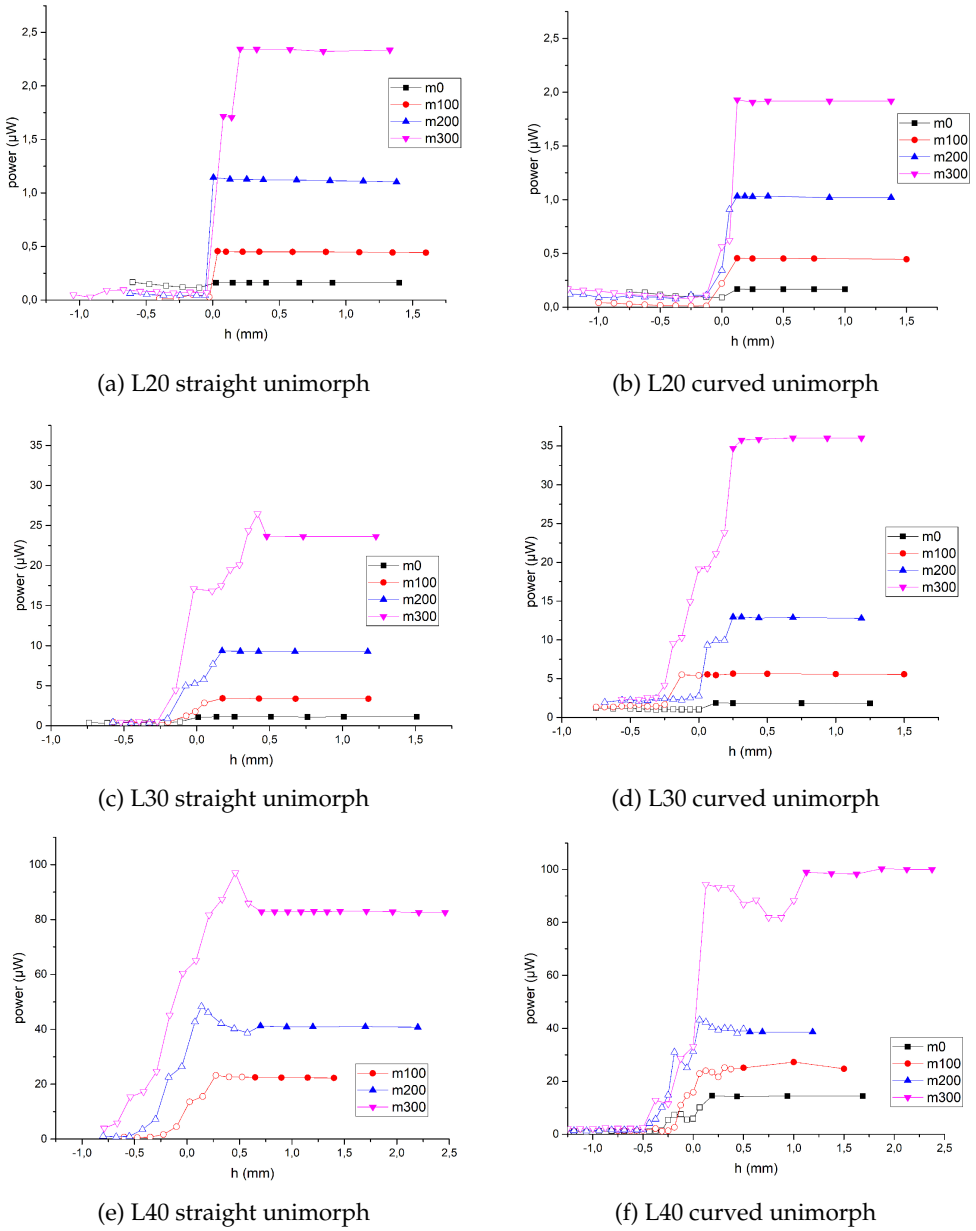

(a) L20 straight unimorph

(b) L20 curved unimorph

(c) L30 straight unimorph

(d) L30 curved unimorph

(e) L40 straight unimorph

(f) L40 curved unimorph

FIGURE 4.16: output power under different stopper distant height, with the filled dots representing vibration without bolt impacts and hollow dots referring the occurrence of impact between unimorphs and bolts

From the results in the previous section, even the largest deflection of 20 mm length unimorph, which was attached with 300 mg tip mass, was still smaller than the precision of the bolt, and therefore the stage of impact was not observable in length 20 mm unimorphs. Besides, unlike the others having gradual output decline in the pre-stressed state, the output value fell directly close to zero once the bolt touched the unimorph. It could be inferred that, due to the high stiffness of the short beams, the force base excitation exerted on the unimorph was no longer sufficient for extra deflection once they had been bent by the bolt, resulting in little output at the pre-stressed state.

On the other hand, small peaks in output at the beginning phase of impact state appeared in some operation condition where samples generated large transverse displacements, such as the straight 30 mm unimorphs with 300 mg tip mass and all the 40 mm unimorphs. Comparing the output waveforms of vibration in different stages, as shown in Fig.4.17, it could be seen that the strikes induced sharp spikes in output waveform. The sharp spikes generated from the impacts lessened along with the reduction in the stopper distance, and even continued decreasing to the state of pre-stressed.

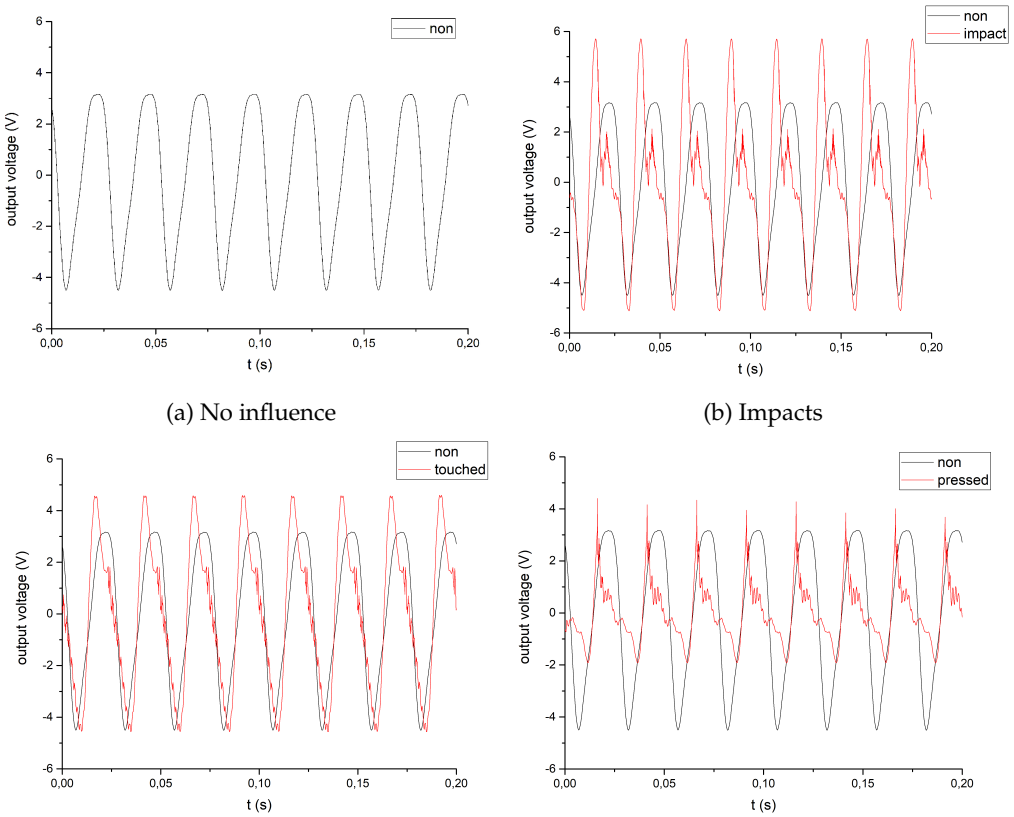

(a) No influence

(b) Impacts

(c) Touched

(d) Pre-stressed

FIGURE 4.17: Output waveform of L40 unimorph with different stopper relation

Two possible causes were used to explain the output peak in the impact state. First, the impact pushed the unimorphs into a more extreme behavior, which had been shown in the steeply risen peak in each waves. Interpret it in the physical vibrational aspect, the stopper limits the motion of the unimorph at one side, but at the same time provides an even larger velocity and displacement to the stopper-free side. Similar behaviors were shown and discussed in the work of Wang et al. (2019)[77]. Another explanation was that the impacts caused the generation of higher frequency vibration, which was were visible on the edge of the right side of the waves on Fig.4.17(c)(d). Those explanations could be observed through logging the displacement of the unimorph tip during vibration. However, they had yet to be proved and the needed to be verified by experiments in the future.
From the previous figure (Fig.4.16), it could be seen that not all the initiate sharp spikes caused by the strokes improve the average power output, only those samples with sufficiently small stiffness leads to an increase. It was also unknown to what

extent the peak values of the spikes in Fig.4.17 reducing to would the average power output drop below the original stroke-free value. As a result, in current stage it could only be found by inspection. Fig.4.18 was made to show the generated energy accumulation from the vibration over 0.25 second with different stopper distances of a L30 straight unimorph with a tip mass 200 mg. It could be found that there is no linear relation between the stopper distance and the energy output, and larger output happens at the region where the peaks in Fig.4.16 are. However, neither the region of output increase nor the maximum position is certain or has been systematically derived, and this would be another field worth further investigation in the future.

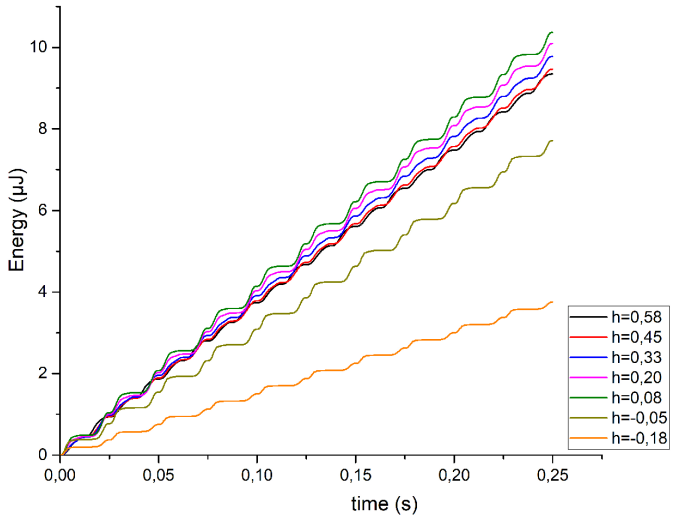

FIGURE 4.18: Accumulated energy output over time with different limit stop distance

But, as what had been discussed previously, the larger output resulted from the impact might due to the more extreme behavior of the unimorph, and to know whether this was really “optimal”, lifetime experiments were needed.

4.4 Exp 2 - Lifetime Performance Analysis

Results from previous experiments have stated that there were no significant differences in output behavior between the straight and curved unimorphs. Considering that there were still plenty of unknowns and uncontrollable factors about the curved unimorphs, such as the curvature, the internal stress, to name but a few, only the straight unimorphs were tested for the life time experiments, and assumed that the curved unimorphs would behave similarly.

Failure behavior

General long term fatigue failure behaved as Fig.4.19 displays. The straight red line in the figure represents point a breakage. As the unimorph breaks, it first shows instability in performance, and then a trend in increase in output voltage peak-to-peak while a decrease in root-mean-square value. This incident could be more clearly explained as one look into the waveform of a broken unimorph (Fig.4.20). The broken sample displays sharp spikes in its output waveform, and the rising side of the wave is broken into small, high frequency waves.

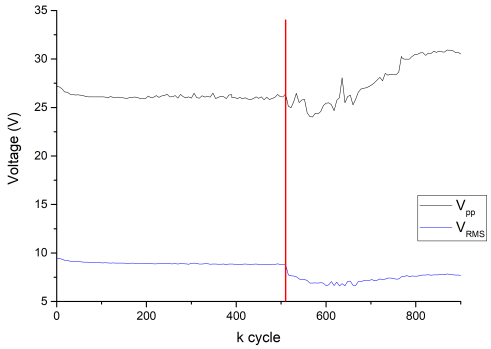

FIGURE 4.19: Output voltage changes upon breakage

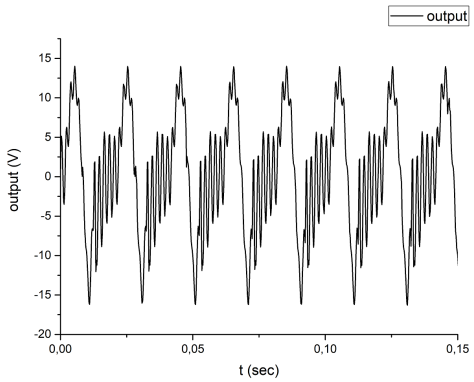

FIGURE 4.20: Output waveform of a broken unimorph

4.4.1 lifetime versus tip mass

Unimorphs with tip mass from 200 to 300 mg were tested for long term performance, and the results are shown in Fig.4.21. In the figure, the y axis is the natural logarithm of the number of total life cycle, and the x axis is the mass attached at the unimorph tip. Filled dots denote the experimental data, with the thick dash-dot line being their trend line. It could be observed that the life length shortens along with the increase in mass, and the direct relation was derived to be $T \propto m^{-22.67}$, where T denotes the total life cycles. The red line in the figure indicates the cycle number of literally one day, and it has been calculated that the lifetime of the unimorph is exactly one day when having a tip mass of 209 mg. The hollow dots, on the other hand, refer to those lifespan exceeding one day, which are regarded as having infinite service time. Therefore, a straight dash line is extended from the intersection of the trend line and one day line, which is known to be where 209 mg positions, indicating the life length of tip mass lighter than 209 mg is infinite. In addition, the intersection of the trend line and the x-axis occurs at 381.7 mg, implying that the lifetime is nearly zero as the

tip mass exceeds 381.7 mg, and the sample is expected to break immediately once it starts vibration.

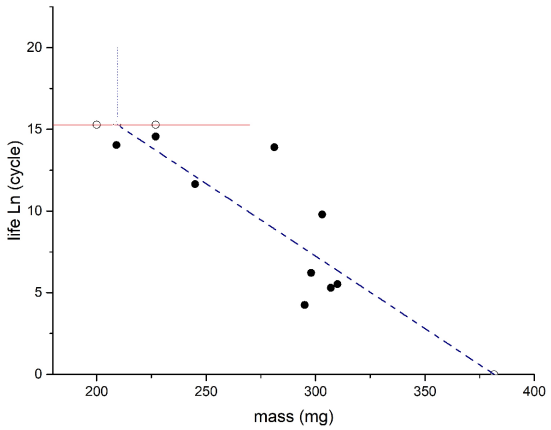

FIGURE 4.21: Total life cycle v.s mass

4.4.2 lifetime versus stopper distance

The second part of the lifetime experiments studied the effect of the stopper distance on the life time of the unimorph operation. Stopper distances of 0.125 mm, 0.25 mm, 0.375mm, 0.5 mm, 0.75 mm, and 1 mm were employed, and the results are displayed in Fig.4.22. The lifetime reduced as the stopper distance increased, and the relation of lifetime to the stopper distance was obtained: $T \propto h^{-1.56}$. The minimum lifetime in this part of experiment is expected to be wherever the h allows the unimorph to perform stroke-free vibration. The distance of the tip deflection derived from the previous trend, here interprets as stroke range, is 1.13 mm, and the corresponding lifespan for stopper located at such distance is around 447 cycles. All the stopper distance larger than 1.13 mm are therefore assumed to have a life around 447 cycles. Also, when $h = 0$ mm, the stopper has direct contact with the unimorph, it was found to have lifetime of 2.26M cycles.

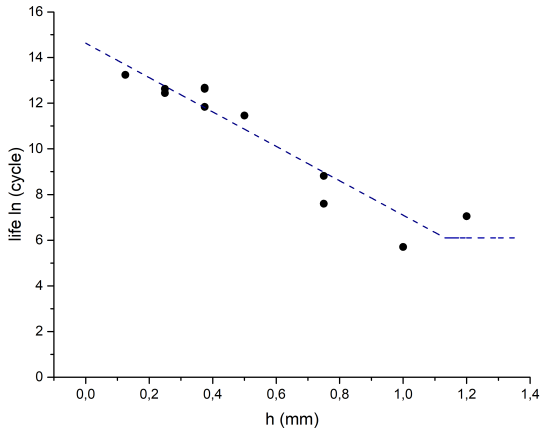

FIGURE 4.22: Total life cycle v.s stopper distance

The phenomena above are reasonable because unimorphs subjected to larger cyclic strain are more prone to mechanical failure. Larger tip mass and larger stopper distance, in general, allow greater unimorph deflection during vibration. When the unimorph is less movable due to less tip mass or motion constrained by stoppers, the stresses in the unimorphs has become less and consequently able to last for longer.

4.4.3 Performance comparison

Previous section has indicated the difference in trend from lifetime performance, which declines in most of the measures improving the output. However, the significance of these domains on the overall performance is yet to be known. This section aims to first compare the results from the previous section with power output, and then discuss the benefits and trade-off of performance in output and lifetime of unimorphs.
Fig.4.23(a) presents the same experiments conducted in section 4.4.1 while in the view of energy output. It can be observed that power output has an inverse trend to the lifetime, being positive correlated to the tip mass, and the relation of the power output to the tip mass was found, by taking logarithm to both parameters, $P \propto m^{0.29}$. Power capacity is then introduced to help further understand the effect of the two domains, as shown in Fig.4.23(b). Power capacity, E_{life}, denoting the total energy generated during the entire service life of a power source, the unimorph function life in our case, is the product of power output and the total lifetime. It could be observed that, even though unimorphs with larger tip masses offered larger instant power output, the power capacity they provided was less than those with small tip masses. In other words, the margin of the increase in power was far less than that of the decrease in lifetime. This could also be clarified by the previously found trends in the two parameters, which the relation of power capacity to tip mass was the multiplication of the two. The exponent to the tip mass equals to the sum of the two exponents, $E_{life} \propto m^{-22.38}$, ended up resulting in a large negative number.

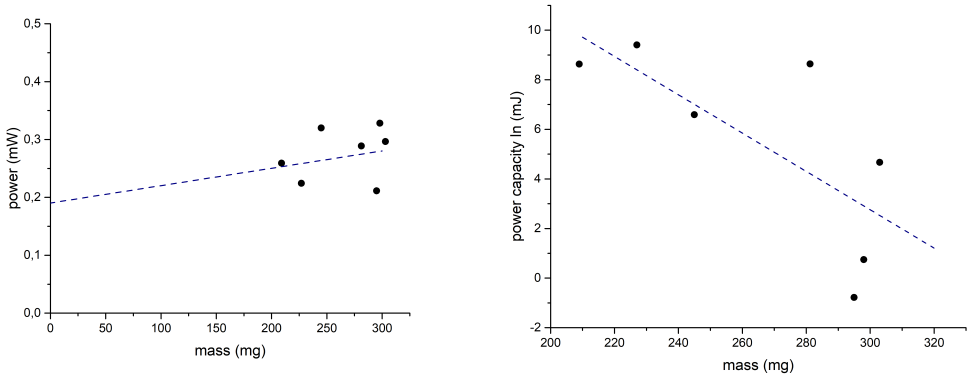

(a) Power generated v.s mass

(b) Power capacity v.s mass

FIGURE 4.23: Lifetime and power capacity of unimorphs with different tip mass

Following the same procedures, experiment results in 4.4.2 were also plotted into Fig.4.24(a). Likewise, the power output, opposite to lifetime, has a positive correlation with stopper distance, in a relation of $P \propto h^{0.29}$. This resulted to the trend of $E_{life} \propto m^{-1.26}$ in power capacity, shown in Fig.4.24(b). Similar to the previous case, it reveals that the lifetime still dominates the total power capacity of the unimorph, in a relative moderate way.

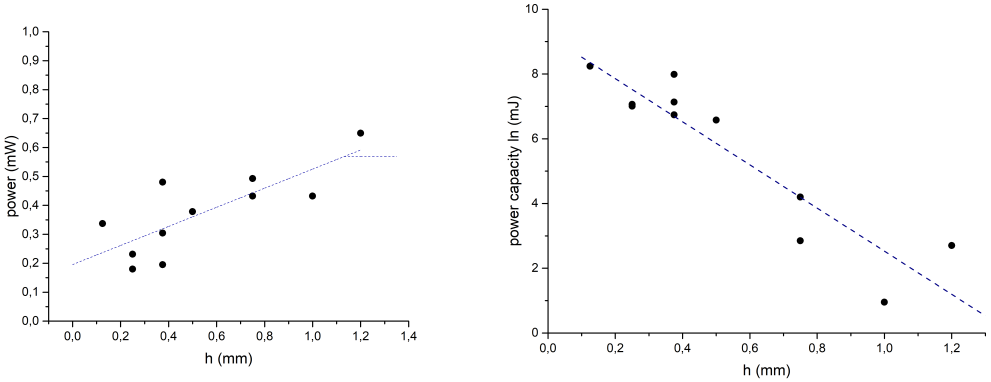

(a) Power generated v.s stopper distance

(b) Power capacity v.s stopper distance

FIGURE 4.24: Lifetime and power capacity of unimorphs with different stopper distance

From the above comparisons, it could be concluded that, while lifetime decreases along with both tip mass and stopper distance increase, the power output in both stroke and stroke-free vibration are in the opposite trend to it, and in a comparatively gradual behavior. In other words, the current design is not able to optimize both output and lifetime at the same time. One ought to choose one optimization from the other. Additionally, the large gap in changing rate is especially obvious when it comes to the combination, the power capacity, of the two. From the trend of the power capacity, one could see power output plays trivial role in the total value determination. Those generate larger instant output could not provide large energy over entire service life for that the lifetime fall too fast.

As the relation between lifetime and power output has already been discovered, the performance between the stroke-free and stroke vibration then come into discussion. In advance to the comparison of those two sets of data, it is first needed to make sure they are comparable. In order to do so, two approaches was done to verify the compatibility of those two sets of data. One is the lifetime matching and the other is power matching.

The purpose of lifetime matching is to ensure that, in the lifetime-distance experiment, when the distance of the stopper exceeds the unimorph maximum deflection, which the unimorph is assumed to undergo stroke-free vibration, the predicted lifetime would match the predicted lifetime in the lifetime-mass experiments with the corresponded tip mass. The tip mass of 320 mg, which was used in the lifetime-distance experiment, was then input to the trend line equation in life-mass experiment, and is demonstrated as the red dot in Fig.4.25(a). The expected life cycle was 240 cycles and the residual to the regression line was 0.6, which was almost the closest to the regression trend among all the others. Therefore, in terms of lifetime, the performances of the two set data are consistent.

As for the output matching, the predicted point at 320 mg from the lifetime-mass

experiment was put into the lifetime-power plot with the data from the second experiment, displayed as the black point in Fig.4.25(b). Even though the results from the second experiment were not close enough to the regression line, it is still observable that the data points with larger stopper distance tend to position at the down-right side. However, the black point, which is the result from stroke-free vibration, is far from where it is expected to be (the down-right part of the figure). As it has been confirmed that the lifetime of the two sets are matched, the position of the black dots also indicate that, under the same life length, the unimorphs from the first experiments generate less power than that of the second.

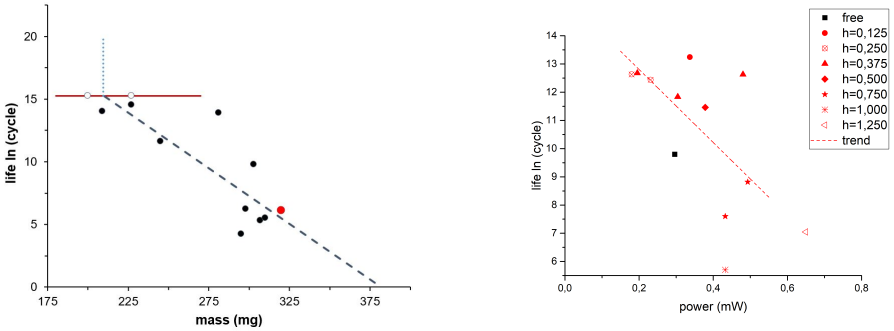

(a) lifetime matching with two sets of data (b) power matching with two sets of data

FIGURE 4.25: Two sets of data matching

The above two approaches show that the two sets of data are not comparable in terms of output due to data mismatched. Nonetheless, their tendencies of changes in under the parameters of power output and life length are still worth discussing. Fig.4.26 presents the relation between the power output and the lifetime in terms of previous two sets of data. This figure also shows the mismatch of the two data. Ideally, the black dots should shift to the right, having the intersection of the two lines occurred at the down-right side of the plot. Besides that, it could be observed that stopper distance has a smaller lifetime decline in response to increment of power output comparing to the tip mass. This also infers that, the stoppers has more influence on the output change, but the influence on the lifetime is not as critical as the tip mass.

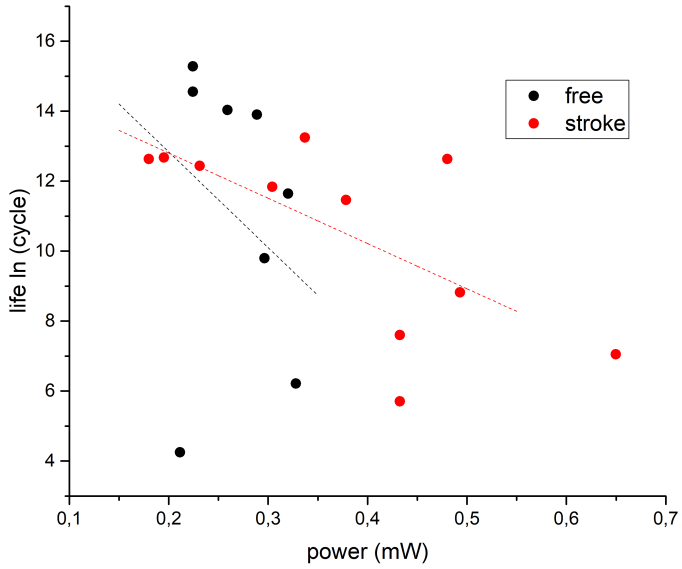

FIGURE 4.26: Comparison of performance trend between stroke-free vibration and vibration with stroke

The above experiments have proved the incompatibility between the two views of performance optimization, which are not able to achieve simultaneously. Regardless that the performance from the stroke and stroke-free vibration are not able to be compared directly, strokes have shown to exert more effects on unimorph power generation while less on lifetime issues. Further tests are expected to be done to obtain comparable data sets for the analysis on performance and benefits brought by the strokes.

Chapter 5

Conclusion

The objective of this project was to optimize the output and lifespan of cantilever-type of energy harvester, also known as unimorph, through the use of a stroke limiter. To realize it, two approaches were chosen. The first was to investigate the change in output produced for various cantilever designs (in size, configuration and attached tip mass) under different limit stopper distances. Secondly, these same conditions were investigated to determine their effects on the lifetime of the unimorph. The results could then be compared to find the optimization of both lifetime and output.
When considering the unimorph configuration, it was found that the design of the unimorph itself still needs optimization as the mechanical neutral line lies within the piezoelectric phase, leading to a reduction in the overall piezoelectric output.
Nevertheless, measurements of the power output of unimorphs were performed by unimorphs of various lengths, configurations, and tip mass, for stroke-free vibration. Stoppers were then added to create a stroke-vibration condition. The findings of this set of experiment are:

- Though the curved unimorphs were expected to generate a larger output, there was no distinct difference in output power for the different configurations. However, the straight unimorphs behaved more consistently with varying length and tip mass than the curved ones;
- The power output and the unimorph length shows a possitive correlation with higher output for longer unimorphs, and the empirical relation of the unimorph length to the power was obtained: $P \propto L^{5.6}$;
- Generally, reducing the stopper distance also led to a nonlinear reduction in the power output of the unimorph. However, for longer unimorph, i.e. 40 mm length, there was a small region at the beginning of the stroke region where the stopper resulted in a larger output signal than the original stroke-free vibration.

For measurement of the lifetime of the harvester with the different experimental conditions, the accelerated method was undertaken. For this, a simplified version of the previous experimental setup was used. The tests focused on straight unimorphs of length 40 mm with the tip mass ranging from 200-320 mg. These results showed a number of things:

- Output and lifetime are negatively correlated. This correlation is particularly steep for the lifetime of the cantilever which decreases more rapidly than the output power increases. In other words, it could be optimized for lifetime without sacrificing too much performance.
- As the power capacity of the unimorph (total energy generated over the lifetime of the harvester) is dominated by the life length of the unimorph, a sharp decrease in this also seen in conditions that increase power output.
- The limit stops and tip masses were found to have opposing effects on the power output and the lifetime. A stopper improved the lifetime of the unimorph while reducing the power output, while a tip mass improved the power output at the expense of lifetime reduction.

Overall, this work shows that stoppers present a useful way to improve the lifetime of a piezoelectric cantilever but at the cost of reducing the power output. Under the specific condition of long cantilevers, they did improve the output but here demonstrated little to no improvement in the lifetime. Our results show that it is still difficult to simultaneously optimize an unimorph with respect to both output and lifetime and that one must rather choose which is more important. High power output designs result in short lifetime and small total power capacity, while longer life designs offer trivial power output. More work is likely needed to find a design that can optimize both.

Chapter 6

Future Development and Recommendation

The work done in the thesis provided a preliminary investigation on lifetime enhancement of energy harvesters, and had left some space for future development. Some modifications to our current design could be made to improve the performance for the future research.
Calculations showed that for our unimorph design, the neutral axis of the cantilever lay within the piezoeletric material, leading to a reduction in overall output as part of the output was canceled within the material. The use of a thicker substrate is advised to avoid this issue. Alternatively, combining two of the current substrates or using a customized substrate could solve this problem.
Apart from changes in sample design, there were some recommendations of areas which merit future exploration:
It was found that, for longer samples, there exists a range of stopper distance where the introductin of the stopper actually improved the power output over the stroke-free value. Currently this range can only be determined empirically, but it is expected that with continued study this could be predicted theoretically and correlated to a range of vibration frequencies or sample conditions.
A change in the placement of the limit stop is recommended for further study. The stopper used in this research was added to the top of the sample and functioned to limit the deflection where the PZT was subjected to compression. As ceramics are known to be weaker in tension than compression, installing the limit stop on the bottom side of the unimorph is expected to be more helpful in protecting the unimorph than at the top, and hopefully could further improve the performance in lifetime.
The effect of stroke on the correlation between lifetime and energy output could not be satisfactorily studied due to the mismatched data. Reproduction of these experiments and obtain more reliable data sets is recommended for future work.
As the design of unimorphs energy harvesters was developed for the end use of incorporation into wearable devices, it is important for the future studies to apply it on human body or test their performance *in-situ* in those device. end use it is still wished to be further put into application on wearable devices. It is recommended that the design be considered for incorporation into wrists mounted devices such as watches. As the hands are one of the most frequently moved parts of the human body, the wrist is an ideal location to scavenge energy, especially in the general public who do not take part in strenuous exercise with the same frequency of professional athletes. Incorporation into a watch would allow for local power generation for the watch itself to use.

Bibliography

[1] lu Wang, Jianjun Ding, Zhuangde Jiang, Guoxi Luo, Libo Zhao, Dejiang Lu, Xiao Yang, and Maeda Ryutaro. A packaged piezoelectric vibration energy harvester with high power and broadband characteristics. *Sensors Actuators, A Phys.*, 295:629—636, 2019.

[2] Joana Paulo and Pedro Gaspar. Review and future trend of energy harvesting methods for portable medical devices. volume 2, pages 909—914, 2010.

[3] Steven Anton and Henry Sodano. A review of power harvesting using piezoelectric materials (2003-2006). *Smart Mater. Struct.*, 16(3), 2007.

[4] Joseph Paradiso and Thad Starner. Energy scavenging for mobile and wireless electronics. *IEEE Pervasive Comput.*, 4(1):18—27, 2005.

[5] Mohsen Safaei, Henry A Sodano, and Steven R Anton. A review of energy harvesting using piezoelectric materials: State-of-the-art a decade later (2008-2018). *Smart Mater. Struct.*, 28(11), 2019.

[6] Rupesh Patel. *Modelling analysis and optimisation of cantilever piezoelectric energy harvesters*. PhD thesis, 2013.

[7] Shad Roundy, Paul Wright, and J.M. Rabaey. A study of low level vibrations as a power source for wireless sensor nodes. *Comput. Commun.*, 26(11), 2003.

[8] Pim Groen. *An Introduction to Piezoelectric Materials and Applications*. Apeldoorn: Stichting Applied Piezo, 2013.

[9] Shaul Katzir. The Discovery of the Piezoelectric Effect. In *The Beginnings of Piezoelectricity - A Study in Mundane Physics*, volume 57, pages 61—91. Dordrecht: Springer, 2003.

[10] IEEE Standards Board. Ieee standard on piezoelectricity. Standard ANSI/IEEE Std 176-1987, Institute of Electrical and Electronics Engineers, New York, US, 1988.

[11] Chris Bowen, H Alicia Kim, P. Weaver, and Steve Dunn. Piezoelectric and ferroelectric materials and structures for energy harvesting applications. *Energy Environ. Sci.*, 7(1):25—44, 2014.

[12] Kenji Uchino. Piezoelectric Energy Harvesting Systems—Essentials to Successful Developments. *Energy Technol.*, 6(5):829—-848, 2018.

[13] Z. Yang, Shengxi Zhou, J. Zu, and D. Inman. High-Performance Piezoelectric Energy Harvesters and Their Applications. *Joule*, 2(4):642—697, 2018.

[14] Huidong Li, Chuan Tian, and Zhiqun Deng. Energy harvesting from low frequency applications using piezoelectric materials. *Appl. Phys. Rev.*, 1(4), 2014.

[15] Fundamentals of Piezoelectricity. In *Piezoelectric Transducers for Vibration Control and Damping*, Advances in Industrial Control, pages 9–35. Springer, London, 2006.

[16] Shashank Priya. Advances in energy harvesting using low profile piezoelectric transducers. *J. Electroceramics*, 19(1):165—-182, 2007.

[17] Gongbo Zhou, Linghua Huang, Wei Li, and Zhencai Zhu. Harvesting ambient environmental energy for wireless sensor networks: A survey. *J. Sensors*, 2014, 2014.

[18] Kenji Uchino. Piezoelectric ceramics for transducers. In *Ultrasonic Transducers–Materials and Design for Sensors, Actuators and Medical Applications*, Electronic and Optical Materials, chapter 3, pages 70–116. Woodhead Publishing Limited, 2012.

[19] Piezoelectric PZT Ceramics. In *Piezoelectricity*, volume 114 of *Materials Science*. Springer, Berlin, Heidelberg, 2008.

[20] Paul Mitcheson, Eric Yeatman, G. Rao, Andrew Holmes, and Tim Green. Energy harvesting from human and machine motion for wireless electronic devices. *Proc. IEEE*, 96(9), 2008.

[21] Rodrigo Ai, Luciana Monteiro, Paulo Monteiro Jr, Pedro Pacheco, and Marcelo Savi. Piezoelectric vibration-based energy harvesting enhancement exploiting nonsmoothness. *Actuators*, 8(1), 2019.

[22] C.B. Williams and R.B. Yates. Analysis of a micro-electric generator for microsystems. *Sensors Actuators A Phys.*, 52(1–3), 1996.

[23] Jessy L Baker, S. Roundy, and P. Wright. Alternative geometries for increasing power density in vibration energy scavenging for wireless sensor networks. In *EC-12: Advanced Converter Technology*, volume 2, pages 959–970, August 2005.

[24] Isaku Kanno. Piezoelectric MEMS for energy harvesting. *MRS Bull.*, 37(11), 2012.

[25] Daniel J. Inman and Shashank Priya. *Energy Harvesting Technologies*. Springer, US, 2009.

[26] A. Lenk, Rüdiger Ballas, Roland Werthschützky, and G. Pfeifer. *Electromechanical Systems in Microtechnology and Mechatronics-Electrical, Mechanical and Acoustic Networks, their Interactions and Applications*. Microtechnology and MEMS. Springer, Berlin, Heidelberg, 2011.

[27] Waleed Al-Ashtari, Matthias Hunstig, Tobias Hemsel, and Walter Sextro. Frequency tuning of piezoelectric energy harvesters by magnetic force. *Smart Materials and Structures*, 21(3):035019, 2012.

[28] Zhengbao Yang, Alper Erturk, and Jean Zu. On the efficiency of piezoelectric energy harvesters. *Extreme Mechanics Letters*, 15:26 – 37, 2017.

[29] Elie Lefeuvre, Adrien Badel, Claude Richard, and Daniel Guyomar. Piezoelectric energy harvesting device optimization by synchronous electric charge extraction. *Journal of Intelligent Material Systems and Structures*, 16(10):865–876, 2005.

[30] Y C Shu and I C Lien. Analysis of power output for piezoelectric energy harvesting systems. *Smart Materials and Structures*, 15(6):1499–1512, 2006.

[31] Adam M. Wickenheiser and Ephrahim Garcia. Power optimization of vibration energy harvesters utilizing passive and active circuits. *Journal of Intelligent Material Systems and Structures*, 21(13):1343–1361, 2010.

[32] Abdul Alameh, Mathieu Gratuze, Mohannad Elsayed, and Frederic Nabki. Effects of proof mass geometry on piezoelectric vibration energy harvesters. *Sensors*, 18(5):1584, 2018.

[33] A. Erturk and D.J. Inman. On mechanical modeling of cantilevered piezoelectric vibration energy harvesters. *Journal of Intelligent Material Systems and Structures*, 19(11):1311–1325, 2008.

[34] Yu Jia and Ashwin.A. Seshia. Power optimization by mass tuning for mems piezoelectric cantilever vibration energy harvesting. *Journal of Microelectromechanical Systems*, 25(1):108–117, 2016.

[35] Mikio Umeda, Kentaro Nakamura, and Sadayuki Ueha. Analysis of the transformation of mechanical impact energy to electric energy using piezoelectric vibrator. *Japanese Journal of Applied Physics*, 35(Part 1, No. 5B):3267–3273, 1996.

[36] Lei Gu and Carol Livermore. Impact-driven, frequency up-converting coupled vibration energy harvesting device for low frequency operation. *Smart Materials and Structures*, 20(4), mar 2011.

[37] Lei Gu. Low-frequency piezoelectric energy harvesting prototype suitable for the mems implementation. *Microelectronics Journal*, 42(2):277–282, 2011.

[38] Tzeno Galchev, Hanseup Kim, and Khalil Najafi. A parametric frequency increased power generator for scavenging low frequency ambient vibrations. *Procedia Chemistry*, 1(1):1439–1442, 2009.

[39] Tzeno Galchev, Ethem Aktakka, and Khalil Najafi. A piezoelectric parametric frequency increased generator for harvesting low-frequency vibrations. *Microelectromechanical Systems, Journal of*, 21:1311–1320, 12 2012.

[40] Lokesh Dhakar, Huicong Liu, Francis Tay, and Chengkuo Lee. A new energy harvester design for high power output at low frequencies. *Sensors Actuators A. Phys.*, 199:344–352, 2013.

[41] Michele Pozzi. Analytical modelling of a plucked piezoelectric bimorph for energy harvesting. 03 2012.

[42] P. Pillatsch, Eric Yeatman, and A. Holmes. Magnetic plucking of piezoelectric beams for frequency up-converting energy harvesters. *Smart Materials and Structures*, 23, 01 2014.

[43] Arunas Kleiva and Rolanas Dauksevicius. Numerical and experimental study of a novel body-mounted piezoelectric energy harvester based on synchronized multi-magnet excitation. pages 1–6, 03 2019.

[44] R. M. Tieck, G. P. Carman, and D. G. Enoch Lee. Electrical Energy Harvesting Using a Mechanical Rectification Approach. volume Aerospace of *ASME International Mechanical Engineering Congress and Exposition*, pages 547–553, 11 2006.

[45] Adam Wickenheiser and E Garcia. Broadband vibration-based energy harvesting improvement through frequency up-conversion by magnetic excitation. *Smart Materials and Structures*, 19:065020, 05 2010.

[46] Matthew Malkin and Christopher Davis. Multi-frequency piezoelectric energy harvester. *Journal of The Acoustical Society of America - J ACOUSTSOC AMER*, 118, 01 2005.

[47] Marco Ferrari, Vittorio Ferrari, Michele Guizzetti, Daniele Marioli, and Andrea Taroni. Piezoelectric multifrequency energy converter for power harvesting in autonomous microsystems. *Sensors and Actuators A: Physical*, 142:329–335, 03 2008.

[48] Zengtao Yang and J. Yang. Connected vibrating piezoelectric bimorph beams as a wide-band piezoelectric power harvester. *Journal of Intelligent Material Systems and Structures*, 20:569–574, 2009.

[49] G. Lesieutre and C. L. Davis. Can a coupling coefficient of a piezoelectric device be higher than those of its active material? *Journal of Intelligent Material Systems and Structures*, 8:859 – 867, 1997.

[50] Eli Leland and Paul Wright. Resonance tuning of piezoelectric vibration energy scavenging generators using compressive axial preload. *Smart Materials and Structures*, 15, 09 2006.

[51] Dylan Morris, John Youngsman, Michael Anderson, and David Bahr. A resonant frequency tunable, extensional mode piezoelectric vibration harvesting mechanism. *Smart Materials and Structures*, 17, 10 2008.

[52] B.P. Mann and N.D. Sims. Energy harvesting from the nonlinear oscillations of magnetic levitation. *Journal of Sound and Vibration*, 319(1):515 – 530, 2009.

[53] Samuel Stanton, Clark Mcgehee, and Brian Mann. Reversible hysteresis for broadband magnetopiezoelastic energy harvesting. *Applied Physics Letters*, 95:174103–174103, 10 2009.

[54] Vinod Challa, Marehalli Prasad, Yong Shi, and Frank Fisher. A vibration energy harvesting device with bidirectional resonance frequency tunability. *Smart Materials and Structures*, 17:15035–10, 02 2008.

[55] Francesco Cottone, H Vocca, and Luca Gammaitoni. Nonlinear energy harvesting. *Physical review letters*, 102:080601, 03 2009.

[56] Shengxi Zhou, Junyi Cao, and Jing Lin. Enhanced broadband piezoelectric energy harvesting using rotatable magnets. *Applied Physics Letters*, 102, 04 2013.

[57] Waleed Al-Ashtari, Matthias Hunstig, Tobias Hemsel, and Walter Sextro. Frequency tuning of piezoelectric energy harvesters by magnetic force. *Smart Materials and Structures*, 21, 02 2012.

[58] Todd A. Anderson and Daniel W. Sexton. A vibration energy harvesting sensor platform for increased industrial efficiency. In Masayoshi Tomizuka, Chung-Bang Yun, and Victor Giurgiutiu, editors, *Smart Structures and Materials 2006: Sensors and Smart Structures Technologies for Civil, Mechanical, and Aerospace Systems*, volume 6174, pages 621 – 629. International Society for Optics and Photonics, SPIE, 2006.

[59] Shad Roundy, Eli Leland, Jessy Rivest, E. Carleton, Elizabeth Reilly, E. Lai, B. Otis, J.M. Rabaey, P.K. Wright, and V. Sundararajan. Improving power output for vibration-based energy scavengers. *Pervasive Computing, IEEE*, 4:28 – 36, 02 2005.

[60] Jiang-bo Yuan, Tao Xie, and Wei-shan Chen. Energy harvesting with piezoelectric cantilever. In *2008 IEEE Ultrasonics Symposium*, pages 1397–1400, 2008.

[61] Npl assesses the degradation of piezoelectric materials. *Sensor Review*, 19(3), 1999.

[62] Monika Gall and Bärbel Thielicke. Life-span investigations of piezoceramic patch sensors and actuators. In Marcelo J. Dapino, editor, *Behavior and Mechanics of Multifunctional and Composite Materials 2007*, volume 6526, pages 197 – 208. International Society for Optics and Photonics, SPIE, 2007.

[63] Mitsuhiro Okayasu, Go Ozeki, and Mamoru Mizuno. Fatigue failure characteristics of lead zirconate titanate piezoelectric ceramics. *Journal of the European Ceramic Society*, 30(3):713 – 725, 2010.

[64] Pit Pillatsch, Brian Xiao, Nathan Shashoua, H Gramling, Eric Yeatman, and Paul Wright. Degradation of bimorph piezoelectric bending beams in energy harvesting applications. *Smart Materials and Structures*, 26(3):035046, 2017.

[65] J.A. Brans, Thijs Blad, and N. Tolou. A review of design principles for improved mechanical reliability of cantilever piezoelectric vibration energy harvesters. pages 408–415, 11 2019.

[66] Kanwar Bharat Singh, Vishwas Bedekar, Saied Taheri, and Shashank Priya. Piezoelectric vibration energy harvesting system with an adaptive frequency tuning mechanism for intelligent tires. *Mechatronics*, 22(7):970–988, 2012.

[67] K. H. Mak, S. McWilliam, A. A. Popov, and C. H. J. Fox. Vibro-impact dynamics of a piezoelectric energy harvester. *Structural Dynamics and Renewable Energy, Volume 1 Conference Proceedings of the Society for Experimental Mechanics Series*, pages 273—280, 2011.

[68] M. Soliman, Eihab Abdel-Rahman, and Ehab El-Saadany. A wideband vibration-based energy harvester. *Journal of Micromechanics and Microengineering*, 18, 10 2008.

[69] Dibin Zhu and Stephen Beeby. Kinetic energy harvesting. *Energy Harvesting Systems: Principles, Modeling and Applications*, 01 2011.

[70] Fengxia Wang, Amin Abedini, Turki Alghamdi, and Saeed Onsorynezhad. Bimodal approach of a frequency-up-conversion piezoelectric energy harvester. *International Journal of Structural Stability and Dynamics*, 19(08):1950090, 2019.

[71] Karla Mossi, Zoubeida Ounaies, Ralph Smith, and Brian Ball. Prestressed curved actuators: Characterization and modeling of their piezoelectric behavior. *Proceedings of SPIE - The International Society for Optical Engineering*, 08 2003.

[72] Zdeněk Majer, Oldřich Ševeček, Zdeněk Machů, Kateřina Štegnerová, and Michal Kotoul. Optimization of design parameters of fracture resistant piezoelectric vibration energy harvester. In *Advances in Fracture and Damage Mechanics XVII*, volume 774 of *Key Engineering Materials*, pages 416–422. Trans Tech Publications Ltd, 9 2018.

[73] Shad Roundy, Paul Wright, and J.M. Rabaey. *Energy Scavenging For Wireless Sensor Networks With Special Focus On Vibrations*. 01 2004.

[74] Sanjay Kumar. Comparison of deflection and slope of cantilever beam with analytical and finite element method for different loading conditions. *International Journal of Engineering Science and Innovative Technology (IJESIT)*, 5:45–51, 11 2016.

[75] Noel E. duToit and Brian L. Wardle. Experimental verification of models for microfabricated piezoelectric vibration energy harvesters. *AIAA Journal*, 45(5):1126–1137, 2007.

[76] J. Lagowski, H. C. Gatos, and E. S. Sproles. Surface stress and the normal mode of vibration of thin crystals :gaas. *Applied Physics Letters*, 26(9):493–495, 1975.

[77] Fengxia Wang, Amin Abedini, Turki Alghamdi, and Saeed Onsorynezhad. Bimodal approach of a frequency-up-conversion piezoelectric energy harvester. 2019.